UNIVERSIDAD DE CONCEPCIÓN
FACULTAD DE CIENCIAS FÍSICAS Y MATEMÁTICAS

Mass-Luminosity Anomalies: Evidence of Recent Stellar Interaction in the Extraordinary Blue Straggler S1082?

Anomalías de luminosidad masiva: ¿evidencia de interacción estelar reciente en el extraordinario rezagado azul S1082?

By: Amanda Antonia Quitral Pierart

Thesis presented to the Facultad de Ciencias Físicas y Matemáticas de la Universidad de Concepción to grant grade of Master in astronomy.

Octubre 2025
Concepción, Chile

Profesor Guía: Nathan William Cecil Leigh

ACKNOWLEDGMENTS

I would first like to express my heartfelt gratitude to my advisor, Prof. Nathan Leigh, for his constant encouragement and support throughout this journey. His thoughtful guidance, careful feedback on my writing, and willingness to allow me the freedom to explore my own ideas have been invaluable in shaping both this thesis and my growth as a researcher.

I am also deeply thankful to Prof. Bob Mathieu for his mentorship and wise advice, which have continually inspired me to become a more careful and rigorous scientist. His perspective and generosity with his time have had a profound impact on my work.

To my parents, I owe endless thanks for their unwavering love and support. Your encouragement and warmth have carried me through every stage of this process, and your faith in me has been a source of strength.

I would also like to acknowledge the members of Bob's research group for their collaboration and insights, which greatly enriched this project and made the experience more rewarding.

Finally, to my partner Lukas: thank you for standing beside me through every challenge, for celebrating every small and big milestone, and for your patience and kindness. I cannot thank you enough.

This work was funded by the National Agency for Research and Development (ANID) / Scholarship Program / MAGISTER BECAS CHILE/2023 - 22230322, as well as by financial support from Millenium Nucleus grant NCN2023_002 and via the BASAL Centro de Excelencia en Astrofisica y Tecnologias Afines (CATA) project FB210003.

Resumen

Presento un estudio observacional y teórico del complejo sistema estelar S1082 en el cúmulo abierto M67. Este sistema está formado por al menos cuatro estrellas: una estrella "blue straggler" en una binaria eclipsante de 1,07 días con una estrella de secuencia principal (Binaria A), y otra estrella "blue straggler" en una órbita de 1185 días con una compañera desconocida (Binaria B). Analizé los datos observacionales para obtener los parámetros orbitales y estelares de los componentes del sistema eclipsante. A continuación, exploré escenarios de transferencia de masa y encuentros dinámicos que pudieran explicar las propiedades derivadas de todos los componentes de S1082. Combiné fotometría de alta precisión de K2 y TESS con curvas de luz de archivo, nuevas mediciones de velocidad radial, e imágenes de speckle para refinar los parámetros orbitales y físicos del sistema. Para explorar las vías de formación, realizé simulaciones de evolución binaria con MESA y experimentos de dispersión dinámica con FEWBODY, seguidos de modelos de evolución de mareas. Las soluciones de velocidad radial arrojan masas dinámicas significativamente distintas para la binaria A, con la masa de la estrella secundaria ahora consistente con la masa de "turn-off" del cúmulo. Las imágenes de speckle muestran dos componentes resueltos separados por 390 UA en proyección; en combinación con las dos órbitas espectroscópicas, esto sugiere una configuración cuádruple jerárquica. Concluimos que S1082 A se formó muy probablemente a través de un intercambio dinámico en el que participaron una binaria consistente de una "blue straggler" y una enana blanca, y una intrusa estrella de secuencia principal, seguido de una circularización por mareas. Si A y B están unidos gravitacionalmente, es probable que su emparejamiento se produjera tras su formación independiente, a través de un encuentro dinámico posterior. Este trabajo subraya la importancia de la dinámica estelar en la configuración de la evolución de sistemas estelares complejos dentro de entornos de cúmulos como M67.

Keywords – stars: blue stragglers – stars: individual: S 1082 – open clusters and associations: individual: M67 – master thesis

Abstract

I present an observational and theoretical study of the complex stellar system S1082 in the open cluster M67. This system consists of at least four stars: a blue straggler in a 1.07-day eclipsing binary with a main sequence star (Binary A), and another blue straggler in a 1185-day orbit with an unknown companion (Binary B). I analyzed observational data to obtain the orbital and stellar parameters of the components of the eclipsing system. I then explored mass transfer and dynamical encounter scenarios that could explain the derived properties of all of the components of S1082. I combined high-precision photometry from K2 and TESS with archival light curves, new radial-velocity measurements, and speckle imaging to refine the orbital and physical parameters of the system. To explore formation pathways, I conducted binary evolution simulations with MESA and dynamical scattering experiments with FEWBODY, followed by tidal evolution modeling. My revised radial-velocity solutions yield significantly changed dynamical masses for Binary A, with the secondary mass now consistent with the cluster turnoff mass. Speckle imaging shows two resolved components separated by 390 AU in projection; in combination with the two spectroscopic orbits, this is suggestive of a hierarchical quadruple configuration. I conclude that S1082 A most plausibly formed through a dynamical exchange involving a BSS–WD binary and a MS intruder, followed by tidal circularization. If A and B are gravitationally bound, their pairing likely occurred after their independent formation, through a subsequent dynamical encounter. This work underscores the importance of stellar dynamics in shaping the evolution of complex stellar systems within cluster environments such as M67.

Keywords – Template, NHH, master thesis, LaTeX

Contents

List of Tables

List of Figures

Chapter 1

Introduction

It is now widely accepted that the evolution of many Sun-like stars cannot be explained by single-star evolution alone (Mathieu and Pols, 2025). Observations often show their origins to be clearly associated with evolutionary processes in binary environments. One such class of stars are blue straggler stars (BSSs), first discovered in the globular cluster M3 (Sandage, 1953) and the open cluster M67 (Johnson and Sandage, 1955). These are stars that have gained mass during their main sequence (MS) evolution and are still undergoing core hydrogen burning. Current theories for their origins focus on three mechanisms: mass transfer from an evolved companion in a binary star system (McCrea, 1964; Chen and Han, 2008), mergers of binary stars (e.g., via angular momentum loss in stellar winds or through Kozai-Lidov oscillations in triples, Andronov et al. (2006); Perets and Fabrycky (2009)), and stellar collisions during dynamical encounters (Hills and Day, 1976; Portegies Zwart et al., 2010).

The old open cluster M67 (NGC 2682; 4 Gyr; Balaguer-Núñez et al. (2007)) frequently is used as a canonical example of single-star evolution. However, the CMD of M67 is scattered with kinematic members of the cluster that fall in regions of the CMD not explained by single-star evolution (see Figure 1, Mathieu and Pols (2025)). The BSS S1082 is particularly intriguing. It is a remarkable multiple star system including two BSSs. The system shows complex radial-velocity (RV) and photometric variability, the latter due to an eclipse as well as chromospheric activity and starspots. These features make S1082 a key object for studying binary interactions and BSS formation.

S1082 (ES Cnc, F131, MMJ 6493, WOCS2009) is a bright (V = 11.251, B-V = 0.415) star system located at α = 08:51:20.7915, δ = +11:53:26.168 (ICRS coordinates, J2000). Proper-motion studies have securely shown that S1082 is a member of M67 (Sanders, 1977; Zhao et al., 1993; Geller et al., 2015b). Mathys (1991) first detected a second component in its spectrum. In the same year, Simoda (1991) reported the system to be a photometric variable. Goranskij et al. (1992) found that S1082 hosts a close binary system that has partial eclipses with a period of 1.0677978 ± 0.0000050 days. In the ROSAT study by Belloni et al. (1993), S1082 was detected as one of the brightest X-ray sources in M67. Belloni et al. (1998) suggested that this X-ray activity is generated by active regions on the surface of one of the stars in the binary system. More recently, van den Berg et al. (2004) presented Chandra observations of M67, confirming that S1082 stands out as a bright and variable X-ray source. In addition, Landsman et al. (1998) discovered an excess in the UV emission of the system, from which they suggested that this star has a hot subluminous companion.

van den Berg et al. (2001) (hereafter V01) presented photometric and spectroscopic data for S1082, in which they discovered a third stellar component in the spectrum. They proposed that the system is a hierarchical triple system in which two of the stars are BSSs (one in the inner eclipsing binary and the third star). Sandquist et al. (2003) (hereafter S03) added new photometric data and long-term RV measurements for the third star, finding it to be in an orbit with a period of 1189 days. Without conclusive evidence for a dynamical connection between the third star and the eclipsing system, these authors concluded that S1082 is either a true multiple system containing at least two BSSs or a chance superposition of two BSS cluster members, both having low but comparable probabilities of being correct.

What has made S1082 a particularly notable system are the masses derived by both V01 and S03 for the two stars of the inner (eclipsing) binary. According to S03, the companion star lies on the evolved sequence (MS), but has a mass of 1.6 $M_\odot$, whereas the MS turnoff mass of M67 is 1.3 $M_\odot$ (Geller et al., 2015a). The mass found for the primary BSS was 2.5 $M_\odot$, but the evolutionary track passing through this star in the CMD has a mass of 1.6 $M_\odot$ (Pols et al. (1998), see V01). This suggests that although the star is more massive than the turnoff, it appears underluminous for its inferred dynamical mass, posing a challenge for standard stellar evolution models. The radii of both stars are within their respective Roche

lobes, so S1082 currently is a detached system (V01, S03).

Both V01 and S03 emphasized the challenge of creating the S1082 system and, in particular, the apparently subluminous stars of the inner binary system. S03 suggested that the BSS of the inner binary could have formed from mass transfer between two MS turnoff stars, although the efficiency of mass transfer would have to be very high and the remnant of the donor star would have to be exchanged out of the system. Alternatively, based on energy conservation in stellar interactions, Leigh and Sills (2011) hypothesized that the inner binary system of S1082 formed in a resonant dynamical encounter of two triples, in which multiple collisions occurred.

The system S1082 has been the subject of various recent studies. Pribulla et al. (2008) analyzed light curves (LCs) from the MOST satellite. They assumed a contact binary model for LC fitting, based on mass ratio and temperature estimates from S03. Jadhav et al. (2019) reported S1082 as a bright source in both far-ultraviolet (FUV) and X-ray wavelengths. The authors performed spectral energy distribution (SED) fitting with Kurucz models (Castelli et al., 1997), finding temperatures consistent with S03. They attribute the UV flux to stellar interactions or activity similar to the ones in contact binaries (Jadhav et al., 2019).

The organization of this thesis is as follows. Section 2 introduces the conceptual framework. Section 3 describes the spectroscopic, speckle, and photometric observations used in this study. Section 4 presents the analysis of the revised RV solution, speckle imaging results, light curve modeling and eclipse timing variations. In Section 5 the implications of the observational results are discussed and possible formation pathways for S1082 through numerical modeling were explored, including binary evolution simulations with MESA and dynamical scattering experiments with FEWBODY followed by tidal circularization modeling. In Section 6 I summarize my conclusions.

Chapter 2

Theoretical Framework

2.1 Binary evolution

A large fraction of stars in the Milky Way, especially those of solar-type, are born in binary or higher-order multiple systems (**?**). The evolution of such stars is shaped not only by their internal structure but also by interactions with their companions.

There are two classes of binary systems that are particularly relevant to this study, spectroscopic binaries and eclipsing binaries. In spectroscopic binaries, the orbital motion is detected through periodic Doppler shifts in the spectral lines of one or both stars. In eclipsing binaries, periodic brightness variations are observed as one star passes in front of the other from our line of sight. When combined, spectroscopic and photometric data enable the precise determination of the system's masses, radii, and orbital geometry.

2.1.1 Mass transfer in binary systems

When the stars in a binary system are sufficiently close, they can interact through tidal forces, as well as through mass and angular momentum transfer. In the simplified case of a binary system containing two stars of masses M_1 and M_2 ($M_1 > M_2$), in a circular orbit with separation a, Kepler's third law tells us that

the orbital period P is given by

$$P = \frac{2\pi}{\omega} = 2\pi\sqrt{\frac{a^3}{G\left(M_1 + M_2\right)}}, \tag{2.1.1}$$

where ω is the orbital angular velocity and G is the gravitational constant. Assuming the two stars to be point masses and to have synchronized rotation, then the potential Φ in the rotating system, with the centre of mass at the origin, is given by

$$\Phi = -\frac{q}{1+q}\frac{1}{r_1} - \frac{1}{1+q}\frac{1}{r_2} - \frac{1}{2}\left(x^2 + y^2\right) \tag{2.1.2}$$

where q is the mass ratio, $q = M_1/M_2$, x is the line joining the two stars, y is perpendicular to x in the orbital plane, z is perpendicular to the orbital plane and r_i is the distance to star i, given by

$$r_i = \sqrt{(x - x_i)^2 + y^2 + z^2} \tag{2.1.3}$$

Here $x_1 = 1/(1+q)$, while $x_2 = -q/(1+q)$.

There are five equilibrium points where the potential gradient (eq.2.1.2) is zero, called Lagrangian points. The equipotential passing through the inner Lagrangian point L_1 is crucial in the study of binary stars. It is called the Roche equipotential and it defines a pear-shaped region around each of the two stars, called the *Roche lobe*. The position of the L_1 point is given by

$$x_{L_1} = \frac{1}{1+q} - \left(0.5 + 0.227\,\log q\right). \tag{2.1.4}$$

The Roche lobe radius, R_L, is the radius of a sphere whose volume equals the volume of the Roche lobe itself. An approximate formula for R_L, for all values of q, is

$$R_L = \frac{0.49 q^{\frac{2}{3}}}{0.6 q^{\frac{2}{3}} + \ln\left(1 + q^{\frac{1}{3}}\right)} a. \tag{2.1.5}$$

from Equation 1 in Eggleton (1983). The Roche lobe radius around star 2 is obtained by replacing q by $1/q$.

When both stars are well within their Roche lobes, the system is referred to as *detached*. In this scenario, both stars will mostly maintain a spherical shape and there is a limited interaction between them. However, if the separation between

the stars decreases (thus shrinking the Roche lobes), or if the stars' radii increase due to stellar evolution, one of the stars, typically the most massive one, as it evolves faster, will fill its Roche lobe, adopting a pear-like shape. The system then becomes semi-detached, leading to mass transfer (MT): material flows from the star filling its Roche lobe to its companion through the inner Lagrangian point, L1. This process is known as Roche lobe overflow (RLOF). During conservative MT, all transferred mass is accreted by the companion. However, in real systems, some mass may be lost through winds or outflows, making non-conservative MT more common. In certain cases, e.g. in W UMa binaries, the mass transfer causes both stars to fill their Roche lobes, resulting in a *contact* binary system, where both stars are surrounded by a *common envelope* (Kopal, 1955).

Depending on the evolutionary status of the donor when it experiences RLOF, the mass transfer is classified as Case A, Case B or Case C. These three scenarios correspond to hydrogen burning in the core, rapid core contraction before helium ignition, and the ignition of helium in the core, respectively.

2.1.2 Blue straggler stars

Blue stragglers (BSSs) are stars that have accreted mass during their main sequence phase and are still burning hydrogen in their cores, they are brighter and/or bluer than the main-sequence turn-offs of their stellar cluster population, appearing younger and more massive than expected. Their formation mechanisms are intrinsically linked to binary or dynamical evolution, as single-star models cannot account for their extended lifetimes.

The three main formation scenarios proposed for these stars are mass transfer from an evolved companion, the merger of two main sequence stars, or direct stellar collisions. In the MT scenario, a less evolved star gains mass from a more evolved companion, rejuvenating its core and appearing younger and more massive than the cluster turnoff (McCrea, 1964; Chen and Han, 2008). In the merger scenario, orbital decay or angular momentum loss causes two stars to coalesce (Andronov et al., 2006; Perets and Fabrycky, 2009). In dense stellar environments, direct collisions or resonant interactions may also lead to mergers, forming a rejuvenated star (Hills and Day, 1976; Leonard, 1989; Portegies Zwart et al., 2010). Each of these pathways can lead to a BSS, but the presence of these stars in complex systems such as binaries or quadruples provides additional constraints that help

to distinguish among them.

2.1.3 Dynamical interactions

In stellar clusters, close gravitational encounters between stars are common. Individual stellar interactions affect the dynamics and evolution of clusters (Hut et al., 1992). Mergers affect the host cluster properties, the local density, velocity dispersion, mass function and binary fraction can change during these types of encounters. The outcome of a dynamical interaction depends on the relative velocities, impact parameters, and internal energies of the systems involved. In some cases, an evolved component such as a white dwarf can be replaced by a more massive intruder, forming a new binary configuration. These exchange encounters provide a promising channel for the formation of compact binaries that cannot be explained by isolated evolution.

Chapter 3

Methodology

3.1 Spectroscopic observations

A total of 126 spectroscopic observations were obtained with the former Center for Astrophysics (CfA) Digital Speedometers on both the Multiple Mirror Telescope (MMT[1]) and the 1.5-m Tillinghast Reflector at the Fred Lawrence Whipple Observatory (FLWO). These data revealed low-amplitude radial velocity (RV) variations with a period of 1185 days spanning 5.6 cycles, corresponding to an orbit with an unseen companion. The RVs for this orbital solution were derived using correlation analysis of the Mg b region of the CfA Digital Speedometer spectra (D. Latham, private communication). The individual radial velocities derived are reported in Table 3.1.1, where I list the telescope used ("T" stands for Tillinghast Reflector and "M" for MMT), Barycentric Julian Date, and the radial velocity. The velocity curve is shown in Figure 4.1.2, with orbital parameters reported in Table 4.1.2.

The CfA spectra also showed weak signatures of very broad but shallow lines from the two stars in the 1-day eclipsing binary. A TODCOR analysis yielded a tentative double-lined orbit, but the velocity residuals were large and the results were considered unreliable, likely due to blending with the sharper lines of the primary in binary B. This orbit was therefore not adopted (D. Latham, private communication).

[1]The MMT is operated by the MMT Observatory (MMTO), a joint venture of the Smithsonian Institution and the University of Arizona.

Subsequently, the CfA Digital Speedometers were superseded by the Tillinghast Reflector Echelle Spectrograph (TRES; Szentgyorgyi and Furész 2007), a fiber-fed CCD spectrograph with higher signal-to-noise ratio and wider wavelength coverage.In 2013, an additional 25 high-quality TRES spectra of S1082 were obtained spanning 356 days. These spectra were analyzed with TRICOR (**?**), which models the contributions of all three stars in a triple-lined spectrum and alleviates the blending problem encountered with TODCOR. The preliminary TRICOR analysis was carried out at the CfA by D. Latham and G. Torres (private communication). The best-matching templates adopted were: $T_{\rm eff}$ = 6750 K, $\log g = 4.0$, and $v \sin i = 16$ km s^{-1} for component B; $T_{\rm eff}$ = 7250 K, $\log g = 4.0$, and $v \sin i = 60$ km s^{-1} for star Aa; and $T_{\rm eff}$ = 6000 K, $\log g = 4.0$, and $v \sin i = 80$ km s^{-1} for star Ab. This analysis yielded a convincing double-lined spectroscopic orbit for the eclipsing binary A, shown in Figure 4.1.1, using the velocities for all three stars reported in Table 3.1.2, with orbital parameters listed in Table 4.1.1.

The parameters for this new orbital solution are broadly consistent with those derived from the earlier CfA TODCOR analysis.

Table 3.1.1: CfA Radial velocities for S1082 B

BJD	$v_{\rm rad}$	Telescope	BJD	$v_{\rm rad}$	Telescope
2445062.6545	31.61	T	2446175.7310	36.38	T
2445063.6858	35.69	T	2446176.7309	36.38	T
2445064.6825	36.63	T	2446177.7308	36.42	T
2445098.6570	34.28	T	2446178.7306	36.42	T
2445336.9593	33.55	M	2446179.7305	36.42	T
2445337.9373	34.38	M	2446180.7304	36.42	T
2445338.9242	33.90	M	2446181.7303	36.42	T
2445339.9422	34.22	M	2446182.7302	36.42	T
2445340.9176	35.25	M	2446183.7301	36.42	T
2445341.9348	33.37	M	2446184.7300	36.42	T
2445688.0504	33.94	T	2446185.7299	36.42	T
2445695.9838	33.76	T	2446186.7298	36.42	T
2445713.9625	35.42	T	2446187.7297	36.42	T
2445723.9212	33.64	T	2446188.7296	36.42	T
2446040.9934	35.69	T	2446189.7295	36.42	T

Table 3.1.1: continued.

BJD	v_{rad}	Telescope	BJD	v_{rad}	Telescope
2446042.9886	34.64	T	2446190.7294	36.42	T
2446106.8329	37.81	T	2446191.7293	36.42	T
2446107.8523	37.53	T	2446192.7292	36.42	T
2446108.8858	37.45	T	2446193.7291	36.42	T
2446109.8523	37.51	T	2446194.7290	36.42	T
2446118.8098	36.32	T	2446195.7289	36.42	T
2446119.7707	36.67	T	2446196.7288	36.42	T
2446120.8279	36.94	T	2446197.7287	36.42	T
2446121.8467	36.79	T	2446198.7286	36.42	T
2446124.8397	36.06	T	2446199.7285	36.42	T
2446129.7992	35.42	T	2446200.7284	36.42	T
2446130.8025	35.11	T	2446201.7283	36.42	T
2446133.8116	34.26	T	2446202.7282	36.42	T
2446134.8476	34.63	T	2446203.7281	36.42	T
2446136.8481	36.12	T	2446204.7280	36.42	T
2446137.7426	36.71	T	2446205.7279	36.42	T
2446138.7429	36.53	T	2446206.7278	36.42	T
2446139.7404	36.86	T	2446207.7277	36.42	T
2446140.7779	37.18	T	2446208.7276	36.42	T
2446141.8098	36.79	T	2446209.7275	36.42	T
2446142.8006	36.65	T	2446210.7274	36.42	T
2446144.7756	36.42	T	2446211.7273	36.42	T
2446146.7776	36.29	T	2446212.7272	36.42	T
2446147.7307	36.41	T	2446213.7271	36.42	T
2446148.7311	36.23	T	2446214.7270	36.42	T
2446149.7536	36.74	T	2446215.7269	36.42	T
2446150.7407	36.38	T	2446216.7268	36.42	T
2446151.7505	36.77	T	2446217.7267	36.42	T
2446152.7485	36.35	T	2446218.7266	36.42	T
2446153.7450	36.18	T	2446219.7265	36.42	T
2446154.7447	36.38	T	2446220.7264	36.42	T
2446155.7407	36.38	T	2446221.7263	36.42	T

Table 3.1.1: continued.

BJD	$v_{\rm rad}$	Telescope	BJD	$v_{\rm rad}$	Telescope
2446156.7368	36.40	T	2446222.7262	36.42	T
2446157.7370	36.49	T	2446223.7261	36.42	T
2446158.7331	36.79	T	2446224.7260	36.42	T
2446159.7310	36.12	T	2446225.7259	36.42	T
2446160.7328	36.41	T	2446226.7258	36.42	T
2446161.7346	36.51	T	2446227.7257	36.42	T
2446162.7346	36.48	T	2446228.7256	36.42	T
2446163.7364	36.49	T	2446229.7255	36.42	T
2446164.7357	36.52	T	2446230.7254	36.42	T
2446165.7355	36.50	T	2446231.7253	36.42	T
2446166.7321	36.61	T	2446232.7252	36.42	T
2446167.7338	36.47	T	2446233.7251	36.42	T
2446168.7323	36.64	T	2446234.7250	36.42	T
2446169.7322	36.57	T	2446235.7249	36.42	T
2446170.7319	36.49	T	2446236.7248	36.42	T
2446171.7319	36.43	T	2446237.7247	36.42	T
2446172.7317	36.43	T	2446238.7246	36.42	T
2446173.7314	36.37	T	2446239.7245	36.42	T
2446174.7312	36.38	T	2446240.7244	36.42	T

3.2 Speckle observations

Speckle observations of S1082 were conducted using multiple high-resolution imaging instruments to resolve the individual components of the system. The Differential Speckle Survey Instrument (DSSI, Horch et al. (2009)) was used at two different facilities: first on the 3.5-m WIYN[2] Telescope and later, in 2016, on the 4.3-m Lowell Discovery Telescope (LDT[3]). In addition, observations were obtained

[2]The WIYN Observatory is a joint facility of the NSF's National Optical-Infrared Astronomy Research Laboratory, Indiana University, the University of Wisconsin-Madison, Pennsylvania State University, and Princeton University.

[3]These results made use of the Lowell Discovery Telescope (LDT) at Lowell Observatory. Lowell is a private, non-profit institution dedicated to astrophysical research and public appreciation of astronomy and operates the LDT in partnership with Boston University, the University of Maryland, the University of Toledo, Northern Arizona University and Yale University.

Table 3.1.2: TRICOR radial velocities derived from TRES observations

BJD	$v_{\mathrm{r,\ B}}$	$v_{\mathrm{r,\ Aa}}$	$v_{\mathrm{r,\ Ab}}$
56377.7902	31.90	43.10	25.95
56382.6889	32.26	-24.90	104.28
56399.6892	32.19	16.25	66.28
56405.7535	32.46	137.88	-80.81
56580.9836	35.12	142.96	-98.70
56607.9998	35.84	-29.36	130.83
56622.9808	35.55	-42.38	147.34
56639.9091	35.55	49.98	1.65
56651.0137	36.12	-26.10	138.03
56654.9438	36.30	-13.62	66.34
56655.9452	36.05	37.50	15.82
56656.9461	36.15	65.78	-11.41
56657.9114	36.15	132.69	-94.65
56658.9494	36.16	137.29	-107.99
56659.9281	36.35	148.60	-116.94
56669.9322	36.27	-25.27	142.15
56670.9391	36.07	-1.97	75.09
56671.8604	35.98	94.97	-38.13
56672.8821	36.63	131.78	...
56677.9790	36.46	121.51	-89.73
56678.9411	36.21	68.33	-7.30
56680.9632	36.45	-4.46	56.72
56683.7920	36.24	-17.74	117.16
56724.7487	36.50	-8.55	75.36
56733.7264	36.22	129.60	-84.67

with the NN-EXPLORE Exoplanet Stellar Speckle Imager (NESSI, Scott et al. (2018)), a newer-generation speckle instrument installed at the WIYN Telescope. Additional data were later collected using the Quad-camera, Wave-front-sensing, Six-wavelength-channel Speckle Interferometer (QWSSI, Clark et al. (2020)) at the LDT. These instruments provided high-resolution imaging across a broad range of wavelengths, allowing for precise photometric characterization of the detected stellar components. Regardless of which telescope and instrument was used for a given observation, all data were processed as described most recently in Horch et al. (2021).

To derive the individual B and V magnitudes of the two detected sources, magnitude differences (Δm) were measured across various filters ranging from 467 nm to 880 nm. A total of 20 observations were compiled, and a best-fit linear function was applied using a least-squares minimization approach. The resulting relation between magnitude difference and wavelength allowed interpolation at the central wavelengths of the B (445 nm) and V (551 nm) filters, yielding $\Delta B = 0.254 \pm 0.099$ and $\Delta V = 0.286 \pm 0.104$. Using the known system magnitudes of S1082, $B = 11.647$ and $V = 11.248$, the individual magnitudes of the two components were determined. The primary (brighter) component was found to have $B_A = 12.280 \pm 0.044, V_A = 11.867 \pm 0.045, (B-V)_A = 0.413 \pm 0.063$. The secondary component was derived to have $B_B = 12.534 \pm 0.055, V_B = 12.153 \pm 0.059, (B-V)_B = 0.381 \pm 0.081$.The speckle measurements of the projected separation between the two resolved components are listed in Table 3.2.1.

3.3 Photometric observations

Time-series photometric observations of S1082 have long been challenged by the system's orbital period of very near one day. Single ground-based telescopes, limited to nighttime observations, can only capture portions of the LC during each observing window. This introduces gaps in phase coverage and complicates the identification of eclipse features, especially in a system with such a short orbital cycle. These limitations have been significantly mitigated by recent space-based missions like Kepler/K2 and TESS (Borucki et al., 2010; Howell et al., 2014; Ricker et al., 2015), which provide nearly continuous, high-cadence monitoring

Table 3.2.1: Speckle observations of S1082 from 2012 to 2021.

UT date	Year	PA (°)	Sep (")	Δm	Ctr. Wvl (nm)	Tel.	Inst.
Nov 27	2012	270.2	0.4617	0.00	692	WIYN	DSSI
Nov 27	2012	271.1	0.4627	0.52	880	WIYN	DSSI
Dec 02	2012	270.5	0.4628	0.15	692	WIYN	DSSI
Dec 02	2012	270.7	0.4624	0.33	880	WIYN	DSSI
Dec 11	2013	270.9	0.4605	0.14	692	WIYN	DSSI
Dec 11	2013	270.9	0.4600	0.42	880	WIYN	DSSI
Mar 21	2014	270.9	0.6241	0.37	692	LDT	DSSI
Mar 21	2014	271.0	0.6182	0.49	880	LDT	DSSI
Mar 08	2015	270.9	0.4605	0.40	692	LDT	DSSI
Mar 08	2015	270.7	0.4603	0.55	880	LDT	DSSI
Dec 14	2016	272.3	0.4643	0.35	562	WIYN	NESSI
Dec 14	2016	270.3	0.4583	0.33	832	WIYN	NESSI
Dec 14	2016	272.4	0.4668	0.32	467	WIYN	NESSI
Dec 14	2016	270.3	0.4597	0.30	716	WIYN	NESSI
Feb 25	2021	272.7	0.4634	0.27	880	LDT	QWSSI
Feb 25	2021	273.1	0.4726	0.01	808	LDT	QWSSI

The quadrant of the secondary for the NESSI observations is ambiguous. 180 degrees were added to the measured position angles to match the quadrant of the secondary with the other observations in the table.

over extended periods.

M67, and S1082 specifically, were observed during Campaigns 5, 16, and 18 of the Kepler K2 mission (R. Mathieu, PI), yielding approximately 200 days of photometric data. Observations were made with a cadence of 30 minutes and an exposure time of 30 minutes, using a large $25' \times 25'$ superstamp centered on the cluster. The LCs were extracted and corrected for K2 systematic errors using the CfA light-curve reduction pipeline K2SFF (Vanderburg et al., 2016). The extraction was performed using 20 apertures, and the analysis was conducted using the aperture that yielded the highest photometric precision (Vanderburg and Johnson, 2014). These methods remove systematics caused by the K2 pointing drift. However, some residual long-term instrumental systematics persist and will be addressed in subsequent sections.

Photometric data from the Transiting Exoplanet Survey Satellite (TESS) was also used, which observes each sector of the sky continuously for ∼27 days. S1082 was observed in Sectors 44, 45, and 46 with an exposure time of 10 minutes. Light curves were produced by the MIT Quick-Look Pipeline (QLP; Kunimoto et al.

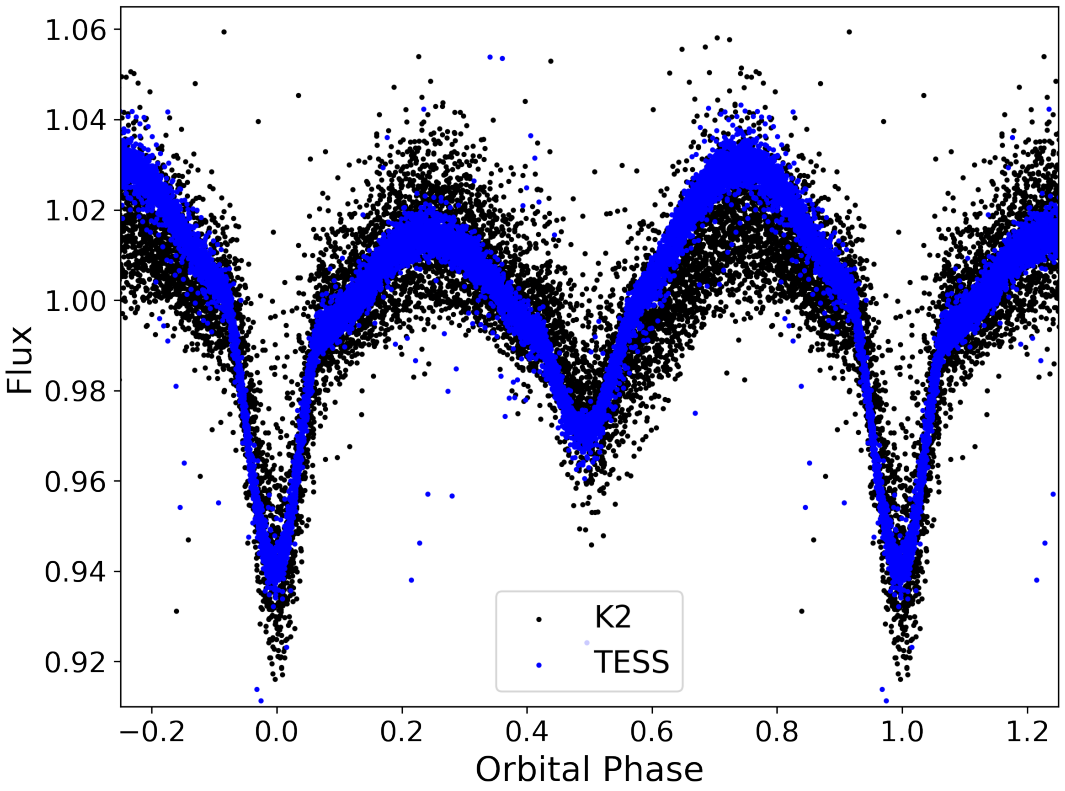

Figure 3.3.1: Light curves of S1082 phased. Black dots are K2 (K2SFF) photometry after differential photometry and flattening, while blue dots are from TESS (QLP).

2022), which extracts photometry from full-frame images using multi-aperture photometry for sources brighter than TESS magnitude 13.5. The pipeline generates flux time series by combining data across the available observations for each target and applies standard detrending methods to mitigate instrumental systematics.

Figure 3.3.1 shows the phased K2 and TESS LCs after applying flattening processes to the K2 data, and using the orbital period ($P = 1.067795$ days) derived in the primary eclipse analysis (see Section 4.3).

3.3.1 Reduction of K2SFF light curves

During the course of data exploration, notable variability was found within the K2 LCs from cycle-to-cycle. This variability manifested both in the long term (month-scale), particularly pronounced in C05 (Figure 3.3.2a), and in the short term (hours-scale), evident as dispersion in C16 and C18.

Hence, to more accurately fit models to the K2 LCs, I applied differential photometry and flattening processes to the S1082 photometric data, allowing me to remove the long-term variability among all three campaigns. Specifically, I divided the LC of S1082 by that of the MS member S1087, which is not intrinsically variable. This star is spatially close, and lies in the same stamp to S1082. The star is sufficiently bright to minimize the contribution of photon (Poisson) noise (Howell, 1989). The differential photometry effectively reduced long-term photometric shifts, most notably in Campaign 5 (Figure 3.3.2b).

However, the phased light curves continued to show low-amplitude low-frequency variation on timescales of many orbital periods across all three campaigns. Subsequent application of a flattening process successfully removed these remaining long-term trends. I performed the flattening with Lightkurve (Lightkurve Collaboration et al., 2018), which has an application called "flatten" that removes the low-frequency trend of a light curve by doing a polynomial fitting using scipy's Savitzky-Golay filter (Virtanen et al., 2020). This resulted in a notable reduction in scattering within the phased LCs (see Figure 3.3.1).

Although the flattening process alone removes most of the long-term instrumental trends in the K2 LCs, I opted to apply differential photometry using the stable cluster member S1087 prior to flattening. This step ensures the correction of low-frequency trends that might not be fully accounted for by flattening. While the LCs processed with and without differential photometry are visually similar, residual analysis reveals structured differences at the millimagnitude level, justifying the inclusion of differential photometry for maximizing precision in the final light curves.

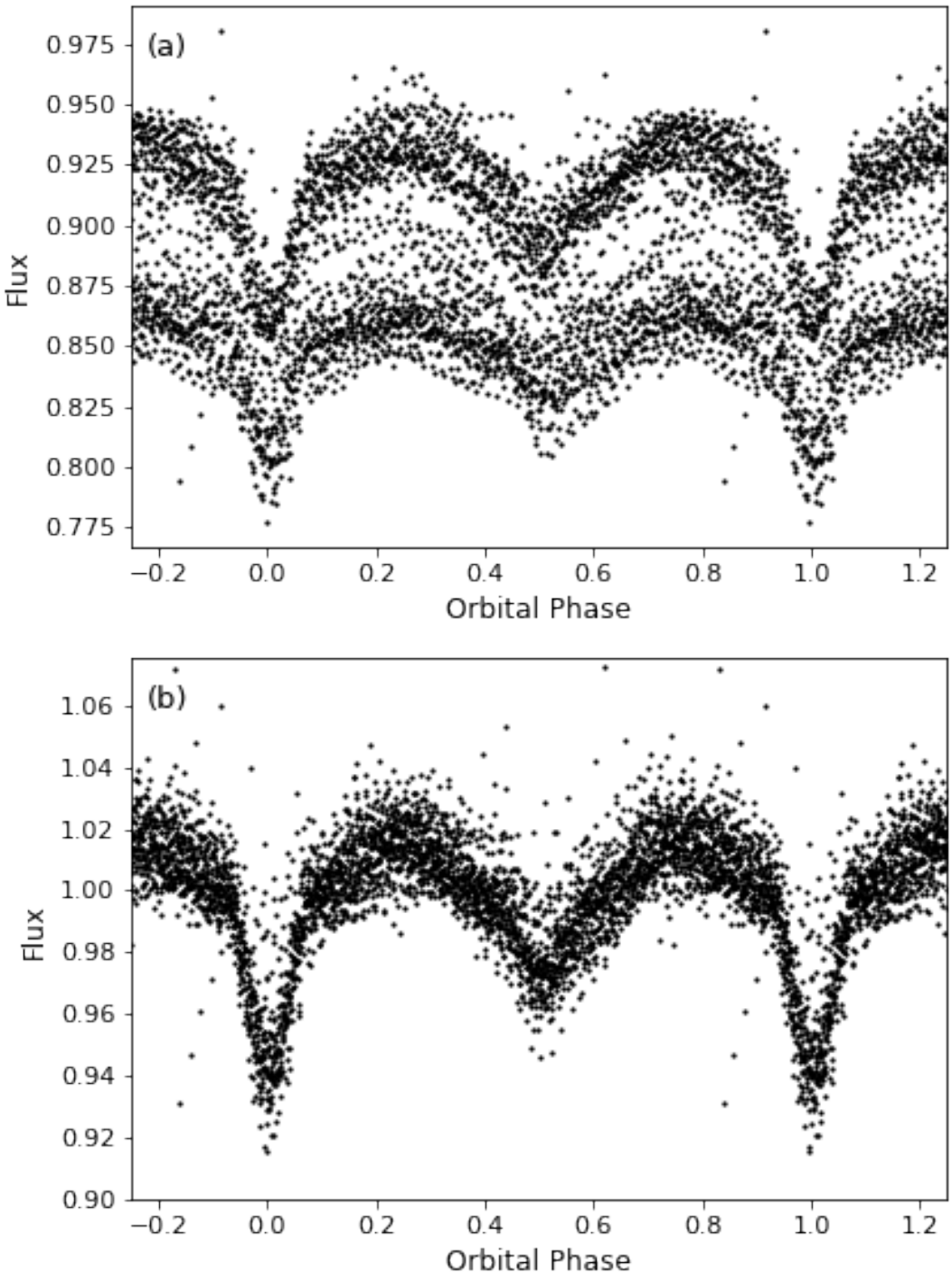

Figure 3.3.2: Light curve of S1082 from K2 campaign 5 before (panel a) and after (panel b) differential photometry using the close-by main sequence star S1087 and flattening.

Chapter 4

Analysis

4.1 Orbital solution

A key result of this study is the revised RV solution for component A in S1082 (Table 4.1.1), which significantly changes the inferred stellar and orbital parameters of the system relative to previous studies. Compared to earlier analyses, particularly that of V01, which reported $M_{\rm Aa}\sin^3 i = 2.01 \pm 0.38$ M$_\odot$ and $M_{\rm Ab}\sin^3 i = 1.26 \pm 0.27$ M $_\odot$, the new solution yields much lower mass estimates of $M_{\rm Aa}\sin^3 i = 1.02 \pm 0.095$ M$_\odot$ and $M_{\rm Ab}\sin^3 i = 0.774 \pm 0.051$ M$_\odot$. Given the measured inclination angle (Section 4.3), this revision brings the mass of the component Ab into closer alignment with the expected values for stars near the turnoff of M67, and thereby decreases the discrepancy that had previously challenged standard evolutionary interpretations.

The quality of the RV measurements is affected by rotational line broadening, particularly in the close binary components. Component Ab shows large velocity residuals ($\sigma_{\rm Ab} \sim 17$ km s^{-1}), consistent with the expectation of rapid rotation. Given the short orbital period ($P_{\rm orb} \sim 1.067$ days), tidal synchronization is likely (Meibom and Mathieu, 2005). Assuming synchronous rotation, the projected rotational velocities were estimated using:

$$v \sin i = \frac{2\pi R}{P} \sin i, \tag{4.1.1}$$

where R is the stellar radius, P is the orbital period, and i is the orbital inclination relative to the observer. Using light curve-derived radii ($R_{\rm Aa} = 1.67$ R$_\odot$, $R_{\rm Ab} =$

Table 4.1.1: Spectroscopic orbit for components Aa and Ab.

Parameter	Value
P_A (days)	1.067799 ± 0.000019
γ_A (km s^{-1})	+37.5 ± 1.1
K_{Aa} (km s^{-1})	109.2 ± 2.2
K_{Ab} (km s^{-1})	143.9 ± 5.9
e_A	0.019 ± 0.015
q_A	0.759 ± 0.032
ω_{Aa} (deg)	59.0 ± 44.
T_A (HJD)	56618.48 ± 0.13
$a_{Aa} \sin i$ (Gm)	1.603 ± 0.033 × 10^6
$a_{Ab} \sin i$ (Gm)	2.113 ± 0.087 × 10^6
$a_A \sin i$ ($R_\odot$)	5.34 ± 0.14
$M_{Aa} \sin^3 i$ ($M_\odot$)	1.020 ± 0.095
$M_{Ab} \sin^3 i$ ($M_\odot$)	0.774 ± 0.051
$N_{obs,\ Aa}$	25
$N_{obs,\ Ab}$	24
σ_{Aa} (km s^{-1})	5.14
σ_{Ab} (km s^{-1})	17.25
$Cycles_A$	333.3

1.77 $R_\odot$), and adopting $i = 66.7°$, I find:

$$v \sin i_{Aa} \approx 72 \text{ kms}^{-1},\ v \sin i_{Ab} \approx 77 \text{ kms}^{-1}. \tag{4.1.2}$$

While no direct $v \sin i$ measurements are available, these values are significantly higher than typical for F-type MS stars. The larger residuals for Ab likely reflect both its slightly higher projected rotational velocity and the increased difficulty in measuring precise RVs from broadened lines.

The new solution for component B also provides a more precise characterization of the orbital parameters (Table 4.1.2). With a larger number of measurements, the uncertainties have been reduced. The new solution indicates a consistent but more precisely constrained period, eccentricity, argument of periastron and velocity semi-amplitude. The new solution is in agreement with S1082 B being part of the cluster, with a systemic velocity of $\gamma_B = +33.679 \pm 0.091$ km s^{-1}, consistent with the cluster mean velocity of +33.64 km s^{-1} (Geller et al., 2015a).

Table 4.1.2: Spectroscopic orbit for narrow-line component B.

Parameter	Value
P_B (days)	1184.539 ± 2.955
γ_B (km s^{-1})	33.679 ± 0.091
K_B (km s^{-1})	2.383 ± 0.182
e_B	0.577 ± 0.059
ω_B (deg)	260.69 ± 6.68
T_B (HJD)	49456.659 ± 13.649
$a_B \sin i$ (Gm)	31.700 ± 2.921
$f(M)_B$ ($M_\odot$)	9.05e–4 ± 2.23e–4
$N_{obs,\,B}$	151
σ_B (km s^{-1})	1.050
$Cycles_B$	9.9

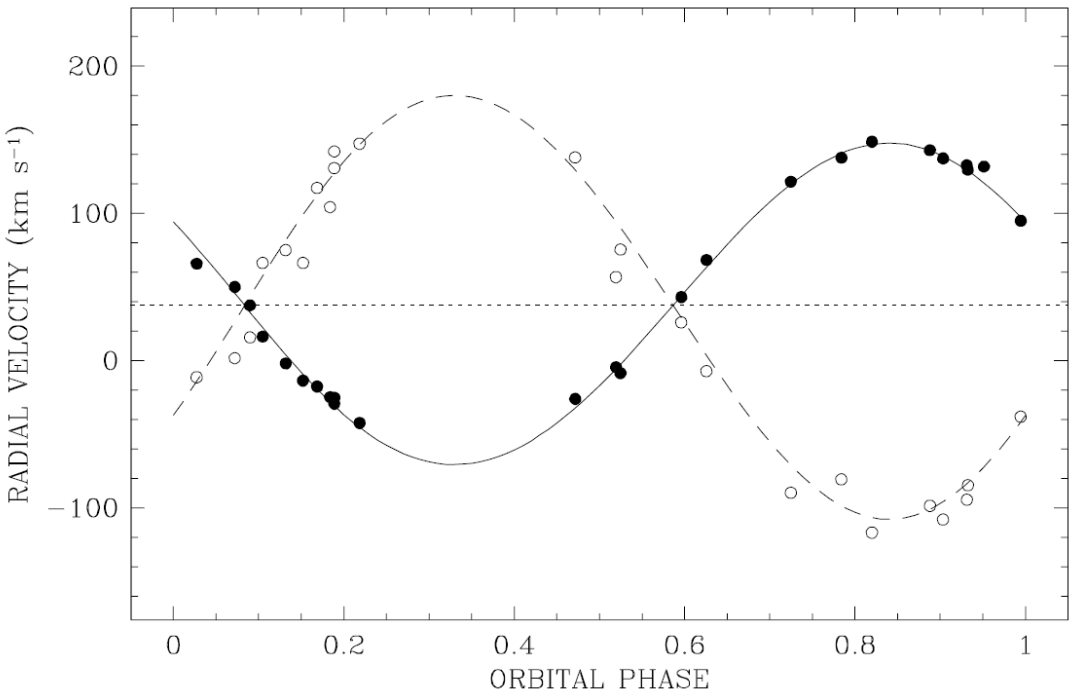

Figure 4.1.1: Phased RV measurements for the eclipsing Binary A, together with the RV curve for the orbital solution. Component Aa is shown as filled circles and component Ab as open circles. The orbital period used to phase the data is 1.067799 days.

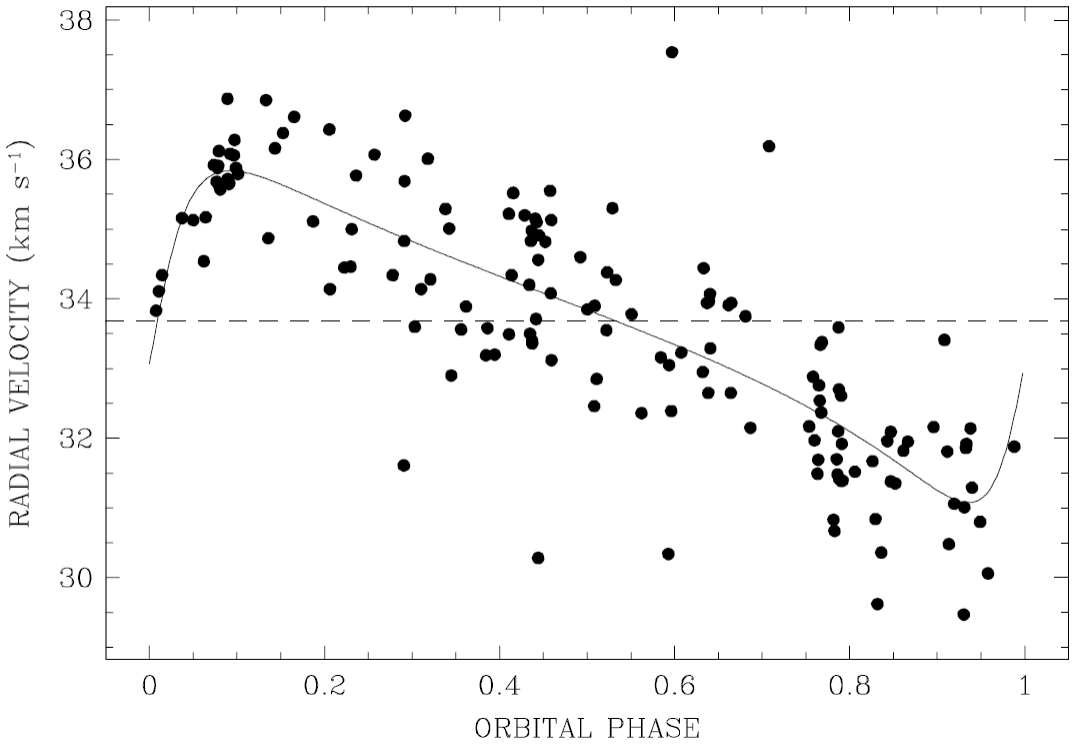

Figure 4.1.2: Phased RV measurements of the binary B, together with the RV curve for the orbital solution. The orbital period used to phase the data is 1184 days.

4.2 Speckle observations analysis

Over a nine-year observational baseline, all speckle images consistently revealed two distinct stellar sources separated by ∼0.463 arcseconds. Assuming a cluster distance of 850 pc (Geller et al., 2015a), this corresponds to a projected separation of 390 AU. No significant change in angular separation or position angle was observed during this period, suggesting negligible relative motion on the timescale of the observations.

The proper motion of S1082 is $\mu_{\mathrm{RA}} = -10.1 \pm 2.2\,\mathrm{mas\,yr^{-1}}$ and $\mu_{\mathrm{DEC}} = -4.2 \pm 1.0\,\mathrm{mas\,yr^{-1}}$ (Zacharias et al., 2013). Over the nine–year span of the speckle observations, this corresponds to a displacement of roughly 90 mas in right ascension, or about twenty percent of the measured separation of the two components. Despite this, the speckle data show no significant relative motion between the two sources. This strongly suggests that A and B are at least co–moving at present. A similar proper–motion approach has been used in other studies to distinguish bound companions from unrelated visual pairs (e.g., Colton et al., 2021). Two Gaia sources are detected at approximately the same separation and position angle as the speckle measurements, consistent with this interpretation, although the current Gaia proper motion uncertainties do not yet allow a definitive confirmation. Future Gaia releases, particularly DR4, may provide stronger constraints.

The implications of these observations are significant. If the resolved components correspond to binary A (the close eclipsing binary) and binary B (the single-lined spectroscopic binary), then the separation and lack of relative motion are incompatible with the 1185-day orbital period inferred for component B. Assuming this separation corresponds to the semi-major axis of the mutual orbit of a hypothetical quadruple system, its orbital period can be estimated using Kepler's Third Law:

$$P_{\mathrm{quad}} = \sqrt{\frac{4\pi^2 a_{\mathrm{wide}}^3}{G(M_{\mathrm{binary}} + M_{\mathrm{wide}})}} \tag{4.2.1}$$

where $a_{\mathrm{wide}} = 390\,\mathrm{AU}$, $M_{\mathrm{binary}} = 2.3\,\mathrm{M}_\odot$ (the mass of the close eclipsing binary),

and $M_{\text{wide}} = 1.76\,\mathrm{M}_{\odot}$ (the mass of the wide binary). Inserting these values yields:

$$P_{\text{quad}} \approx 3800\,\text{years or}\,1.4 \times 10^{6}\,\text{days}.$$

confirming a period three orders of magnitude longer than that of component B. This large discrepancy makes a hierarchical triple scenario dynamically unsustainable.

To test whether the detected pair could be a chance alignment of unrelated stars, the probability of such a superposition within the cluster can be estimated. Assuming a population of 29 BSs in M67 (S03) distributed within a projected radius of 0.9 pc (219 arcsec), consistent with their central concentration reported by Mathieu and Latham (1986), the surface density of BSSs is approximately 1.9×10^{-4} arcsec^{-2}. The area corresponding to a circle of 0.463 arcsec radius is ~ 0.67 arcsec^{-2}, yielding a probability of a random superposition of two BSSs of $\sim 1.3 \times 10^{-4}$, or 0.013%. This estimate is even more conservative than the 0.4% found by S03, who used Monte Carlo simulations to evaluate BSS superpositions within 1 arcsec using the observed radial distribution of BSSs from Sandquist and Shetrone (2003), and would be lower still if using the 16 secure BSS members identified in more recent Gaia-based studies (Leiner and Geller, 2021).

Lastly, the tidal-to-orbital acceleration ratio can be computed to evaluate the potential dynamical influence of the wide binary B on the close binary A. The result, $a_{\text{tidal}}/a_{\text{orbital}} \approx 1.03 \times 10^{-13}$, confirms that tidal effects from B are negligible. Even presuming binaries A and B are physically bound, they evolve independently on very different timescales.

Taken together, the close physical separation observed in speckle imaging, the low probability of a chance superposition, and the independently evolving dynamical behavior all strongly suggest that S1082 A and B are a physically associated pair of binaries in a long-period mutual orbit. If this interpretation is correct, the projected 390 AU separation would correspond to a mutual orbital period of nearly 3800 years, making the system a likely hierarchical quadruple composed of S1082 A (the eclipsing binary) and S1082 B (a single-lined spectroscopic binary). While complete proof of physical association is not yet possible, the likelihood is sufficiently high to motivate treating S1082 as a probable quadruple in the dynamical interaction models explored in Section 5.3.2.1.

4.3 Light curve fitting

Considering that the timescale for intrinsic variations in the shape of the LC is short (even hours), spot activity is very likely (S03). To derive binary parameters for systems such as RS CVn stars there are different methods (e.g., Budding and Zeilik (1987)). The technique used here was similar to that in Pribulla et al. (2008) and S03, where pristine segments were sought.

The description of a pristine segment in this work is a segment with good phase coverage, an equal maximum brightness in the quadratures, an ellipsoidal variation, triangular shaped eclipses, and a brighter mean flux compared to other segments (indicating a time when the surface brightness was least affected by cool starspots, which typically lower the observed flux). A segment with these characteristics should describe a time that minimizes the effects of spots on the structure of the LC.

I did not use TESS LCs to obtain a LC solution because all of the LCs showed clear differences between the two quadrature brightnesses.

The three K2SFF campaigns containing S1082 observations were split into segments of ∼10 days duration to seek pristine segments. After a by-eye inspection, I selected one segment within K2 observations (see Figure 4.3.1). This segment had the lowest dispersion and the clearest structure, fulfilling the conditions mentioned above. But it had a dimmer mean flux during the second quadrature. There are still asymmetries, which unavoidably requires spot modeling.

To obtain a LC solution I did the light curve fitting analysis of the S1082 system using the Eclipsing Binary Learning and Interactive System (ELISa; Čokina et al. (2021) software. Out-of-eclipse variations are modeled in ELISa using Roche geometry to account for tidal distortions, together with reflection effects from mutual irradiation and optional Doppler beaming terms, ensuring that ellipsoidal variability is reproduced consistently with the system's geometry. ELISa initializes the modeling process with user-provided parameters and uses a non-linear large-scale least square trust region reflective (LSTRR) algorithm implemented in SciPy (Virtanen et al., 2020), which allows a quick search for local minima within a predefined search box using a gradient method to fit the photometric data. Following this, it employs the Markov-chain Monte Carlo (MCMC) technique from

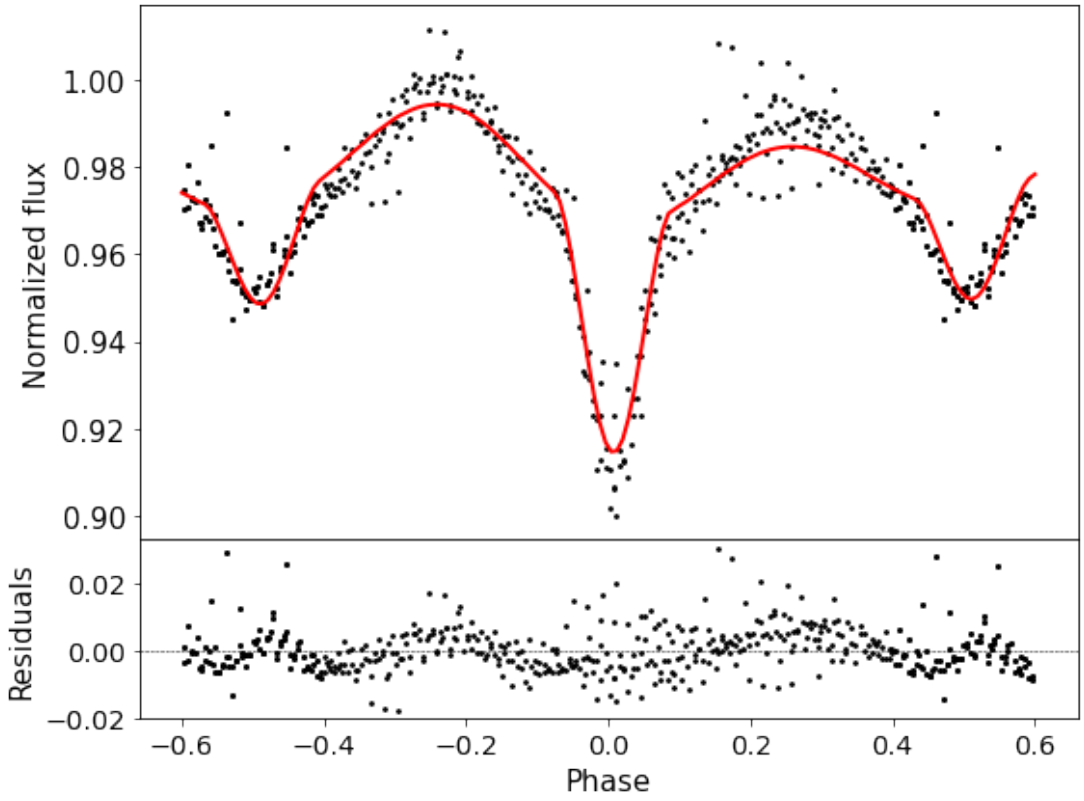

Figure 4.3.1: The chosen "best segment" of the K2 C16 light curve (black dots) and the best fit model (red line). Bottom panel shows the residuals from the fit.

the emcee package (Foreman-Mackey et al., 2013) to explore the parameter space around the preliminary solution, refining the parameter estimates and producing posterior distributions along with corner plots for detailed analysis.

I used as priors the mass ratio, eccentricity and asin i derived in the RV solution. In the initial LSTRR stage, the mass ratio was allowed to vary uniformly within $q = 0.759 \pm 0.032$, and the eccentricity within $e = 0.019 \pm 0.015$. After convergence, q and e were fixed at their best-fit values for the MCMC exploration. The total projected semi-major axis from the RV fit was kept fixed throughout, implemented in ELISa by constraining a through the inclination ($a = 5.34/\sin i$), so that a varied only in response to changes in i during the fit. The effective temperature of star Aa was initially set to 7325 K (as in S03) and then allowed to vary along with the other free parameters. The temperature ratio $T_{\rm Ab}/T_{\rm Aa} = 0.822 \pm 0.031$ is more tightly constrained in the fit than the individual temperatures, consistent with expectations for eclipsing binaries. To account for the difference in brightness between the quadratures following the primary eclipse, I included a single cool

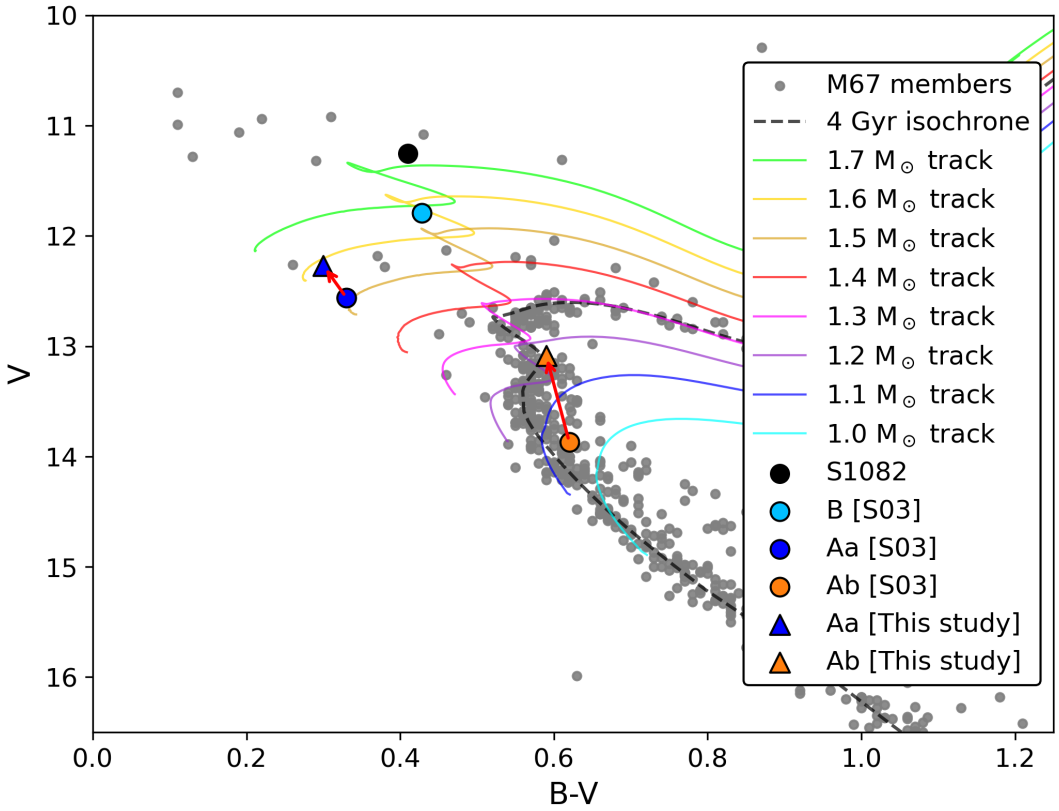

Figure 4.3.2: CMD of M67. Triangles showing my computed positions for the components of the close binary (*blue triangle:* Blue straggler star Aa, *orange triangle:* Main sequence star Ab). Circles show the positions from Sandquist et al. (2003). The red arrows points to the new derived positions of the stars. I overplot a 4.0 Gyr MIST (Dotter, 2016; Choi et al., 2016) isochrone in a black dash-line with a distance of 850 pc, $A_V = 0.093$, and solar metallicity, as well as single-star evolutionary tracks with the same parameters.

spot (longitude = 260º, latitude = 328º, angular radius = 20.6º, temperature factor = 0.8) in the model. Comparable fits could be obtained with the spot placed in other locations, but with only one spot in the model the fit does not reproduce all quadrature structures. Figure 4.3.1 shows the phase-folded LC overlaid with the synthetic model.

Table 4.3.1 shows the derived parameters from the LC solution for the binary A. A significant third light contribution ($l_3 = 0.62$) was identified, consistent with the presence of the binary B. To determine the positions of the stars on the CMD (Figure 4.3.2), I used the effective temperatures and bolometric luminosities derived from the LC solution. ELISa computes the T_{eff} of each component either by fitting it directly as a free parameter (as in this case) or by fixing it based on

Table 4.3.1: Light curve solution for the close binary A. *= from Geller et al. (2015a)

Parameter	This Study	Sandquist et al. (2003)
P (days)	1.0677950799	1.0677971 ± 0.0000007
q	0.759 ± 0.032	0.63 ± 0.04
i (deg)	66.7 ± 0.2	68 ± 1
T_{Aa} (K)	7217.3 ± 9.4	7325 ± 50
T_{Ab} (K)	5930 ± 220	6000 ± 200
R_{Aa} ($R_\odot$)	1.67 ± 0.04	2.04 ± 0.10
R_{Ab} ($R_\odot$)	1.77 ± 0.04	2.15 ± 0.10
M_{Aa} ($M_\odot$)	1.30 ± 0.12	2.52 ± 0.38
M_{Ab} ($M_\odot$)	1.00 ± 0.07	1.58 ± 0.27
l_3	0.6	0.61
V_{Aa}	12.338	12.56 ± 0.03
V_{Ab}	12.934	13.87 ± 0.25
V_{tot}	11.25	11.251
$(B–V)_{Aa}$	0.3	0.33 ± 0.01
$(B–V)_{Ab}$	0.54	0.62 ± 0.07
$(B–V)_{tot}$	0.41	0.415

external constraints, while the L_{bol} is computed assuming blackbody radiation using the Stefan–Boltzmann law. The equivalent radius is obtained numerically from the stellar surface geometry defined by the Roche potential. I converted the ELISa-derived $T_{\rm eff}$ and L_{bol} values into Johnson–Cousins $B-V$ colors and V magnitudes using the bolometric corrections and color–temperature relations in Table 3 of Flower (1996).

The new CMD positions highlight important deviations from single-star evolution. Notably, while component Ab appears more evolved than expected for its ∼1 $M_\odot$ mass at the age of M67, its radius and luminosity are consistent with an evolving MS star nearing the end of hydrogen burning. Conversely, Aa's location supports the interpretation of it being a rejuvenated BSS that has not yet begun post-MS expansion. These CMD placements reinforce the distinct evolutionary histories of the two stars and frame the broader dynamical and evolutionary context explored in the Discussion section **??**.

4.3.1 Eclipse Timing Analysis (O-C Diagram)

With the discovery of component B in the composite light coming from S1082 (V01), the degree of multiplicity of S1082 has been frequently discussed (V01, S03,

Leigh and Sills (2011)). The possibility of a hierarchical triple system between the close binary A and component B could not be proven, because if there is a dynamical connection between them, the reflex motion would be less than the orbital amplitude K of component B (S03).

Nonetheless, in Pribulla et al. (2008) the authors found a high scatter in the photometric O-C diagram, where the deviations were attributed to light-time effects (LITE) caused by component B. However, the derived orbital period did not fit the observed period of the component B orbit, and the results were not conclusive.

Here I present a new analysis of the period variation, together with an updated O-C diagram (Figure 4.3.3) to search for any LITE caused by higher-order multiplicity. (With speckle data component B was discarded as being part of a triple system with A; see Section 4.2). I compiled primary eclipse timings from archival and modern observations, including unpublished Mount Laguna Observatory data, and new timings from K2 and TESS light curves. I segmented the photometric observations into intervals spanning a single orbital cycle. Further filtering was applied to remove cycles that lacked a clearly defined primary eclipse. I did not consider the secondary eclipse, as its shape was more significantly affected by spot activity. The times of primary minimum were determined by following the method described by Deeg (2020) that returns eclipse mid (minimum)-time using the Kwee and van Woerden (1956) method with revised timing error.

Using these timings, I performed a χ^2 minimization over a range of trial orbital periods to identify the best-fit photometric period:

$$P_{\rm timing} = 1.0677951 \pm 0.0000298\,\text{days}.$$

The difference between the RV and photometric period determinations is well within their measurement uncertainties.

To quantitatively assess the deviations in eclipse timings among the different observational datasets, I calculated the mean $O-C$ residual and its associated uncertainty for each dataset, including K2, TESS, and five literature sources. Table 4.3.2 summarizes the mean residuals, root-mean-square (RMS) scatter, and standard error on the mean, defined as $\sigma_{\rm mean} = \text{RMS}/\sqrt{N}$, where N is the number of primary minima measured in each dataset. A dataset was considered to show

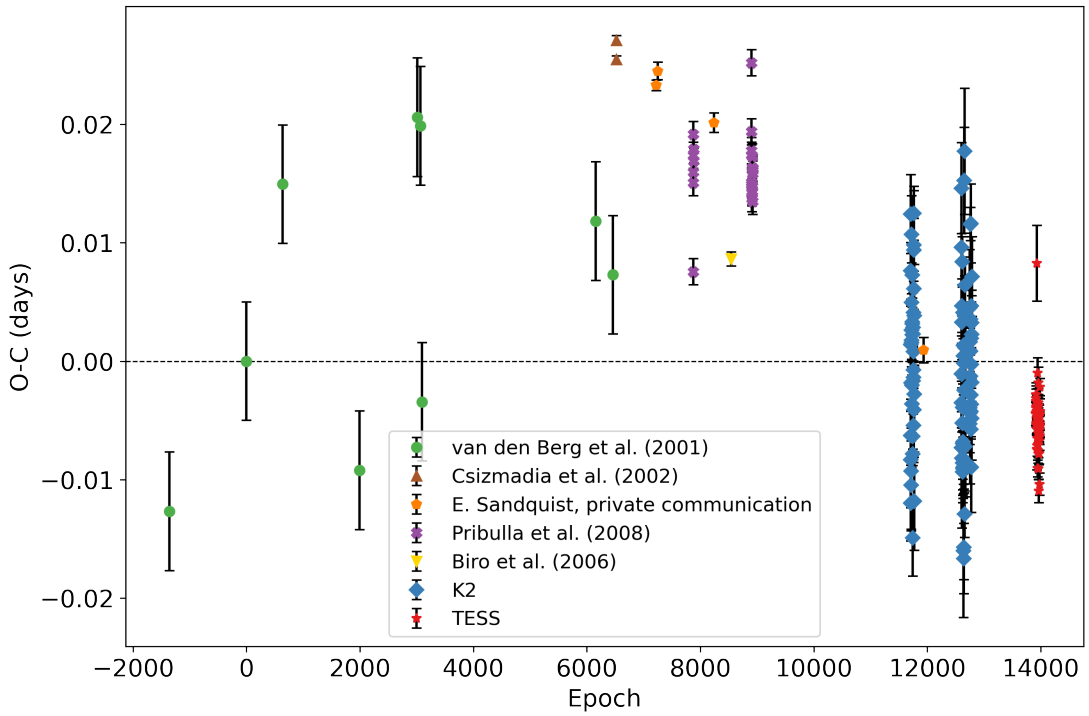

Figure 4.3.3: O-C diagram of the times of the primary eclipse minima for S1082. I consider the same T_0 as van den Berg et al. (2001), 2444643.25 HJD time.

a statistically significant deviation in eclipse timing if the absolute value of its mean $O - C$ residual exceeds $3\sigma_{\text{mean}}$. Based on this criterion, the eclipse timings reported by Csizmadia et al. (2002), E. Sandquist, private communication data, and Pribulla et al. (2008) all show statistically significant positive residuals. These measurements suggest that the primary eclipses in those epochs occurred earlier than expected under the best-fit linear ephemeris. In contrast, The TESS dataset shows a statistically significant negative residual ($\sim 15\sigma$), suggesting that eclipse timings occur earlier than predicted by the linear ephemeris. The K2 dataset is consistent with zero within 3σ, indicating no significant deviation from the timing model.

The light curve of S1082 is characterized by relatively shallow eclipses and a prominent, variable O'Connell effect. The high scatter present in the O-C diagram reflects the complicated determination of precise time minima in such a complex light curve. While these deviations could, in principle, suggest a dynamical origin such as a light-travel time effect from a third companion, I show in Section 5.2 that such an interpretation is inconsistent with independent constraints from radial velocity and speckle observations. The true origin of the period modulation

Table 4.3.2: Statistics of $O - C$ Residuals by Dataset

Dataset	Mean O–C (days)	RMS (days)	Error on Mean (days)	Mean/Error
van den Berg et al. (2001)	0.0055	0.0117	0.0039	1.41
Csizmadia et al. (2002)	0.0263	0.0008	0.0006	43.83
E. Sandquist, private communication data	0.0172	0.0095	0.0048	3.58
Pribulla et al. (2008)	0.0160	0.0029	0.0005	32.00
Biro et al. (2006)	0.0086	0.0000	0.0000	–
K2	−0.0010	0.0073	0.0007	1.43
TESS	−0.0051	0.0026	0.0003	14.88

remains uncertain and likely involves complex stellar processes, which are further explored in the discussion.

Chapter 5

Discussion

5.1 Stellar and Orbital parameters

The RV and LC solutions for the binary A in S1082 confirm several key features of the system's geometry and stellar properties, while also raising notable questions regarding the internal structure and evolutionary state of its components. Compared to earlier work, particularly the solution from V01, the new orbital solution yields notably lower dynamical masses for the stars in binary A. This brings the combined mass of the binary to $\sim$2.3 $M_\odot$, significantly reducing the previous tension with the cluster turnoff mass of 1.3 $M_\odot$. The dynamically measured mass of component Aa is 1.30 $\pm$ 0.12 $M_\odot$, yet its position on the CMD aligns with a single-star evolutionary track of 1.6 $M_\odot$, indicating a 23% discrepancy possibly associated with a non-standard evolutionary history. Similarly, component Ab has a dynamical mass of 1.00 $\pm$ 0.07 $M_\odot$, but its CMD position lies nearer to that of a 1.2 $M_\odot$ track. Although less severe than earlier estimates, this mismatch remains non-negligible.

The filling factors for stars Aa and Ab were calculated using the Eggleton formula (Eggleton, 1983), yielding $R_{Aa}/R_L = 0.71$ and $R_{Ab}/R_L = 0.85$. Most strikingly, the component masses and radii derived from my joint RV and LC analysis yield a configuration in which the more massive BSS Aa appears smaller in radius than its lower-mass MS companion Ab. This size inversion, also reported in earlier studies (e.g., S03), persists in the updated solution despite improved phase coverage, refined RV curves, and high-precision space-based photometry.

Although initially puzzling, this result is consistent with a scenario where Aa has undergone rejuvenation due to mass accretion, delaying its expansion phase, while Ab, potentially a dynamically inserted star, has followed a more typical single-star evolutionary track. This is notable because at the cluster age of M67, a 1.00 $M_{\odot}$ star is not expected to be evolved yet, raising questions about the formation pathway of Ab. The star's parameters may reflect a combination of magnetic activity and rapid rotation, both commonly associated with RS CVn-type binaries. Recent studies (e.g., Cao and Stassun (2025); Morales et al. (2010)) suggest that magnetically active, rapidly rotating low-mass stars can appear inflated in radius and suppressed in effective temperature relative to standard model predictions. The inflation is attributed to starspot coverage and magnetic suppression of convection, which can impede energy transport and cause stellar radii to expand typically by up to 10–15%.

Although my light-curve modeling yields a consistent set of parameters for Ab, I note that the appearance of its eclipses shows some variability across different orbital cycles. In particular, phases centered on the secondary eclipse sometimes show almost continuous brightness changes, with no clear inflection points marking the start or end of the eclipse. This effect could mask the true eclipse geometry and may bias radius determinations toward smaller values when using a "best segment" light curve for modeling. One possible explanation is that ongoing or recent mass transfer, or related circumstellar activity, might be contributing additional variability. If so, the photometric behavior of Ab could be influenced by processes beyond purely geometric eclipses, complicating the interpretation of its radius and temperature and potentially hinting at a more complex interaction history.

In my LC solution I find a synchronicity of 1.038 for both Aa and Ab. My findings agree with S03 in the sense that both stars are rotating asynchronously to the same degree. The orbital eccentricity of the binary A was found to be $0.018^{+0.001}_{-0.0007}$. This supports the idea of the binary being relatively young dynamically, supporting the scenario of dynamical formation, as tidal circularization is expected to already have occurred in such a close binary (Meibom and Mathieu, 2005).

The measured third-light contribution of $l_3 \sim 0.6$ is consistent with the presence of a luminous companion to the binary A. The speckle imaging data presented in this study provide critical constraints on the spatial configuration of the S1082 system.

Across multiple epochs and instruments, the speckle observations consistently reveal two distinct sources separated by $\sim 0.463''$. While I do not perform a direct flux comparison between the third-light fraction derived from the light curve model and the flux of the resolved sources in the speckle images, I do examine their positions on the CMD relative to the photometric properties inferred from my modeling. Based on their relative brightness and color, the brighter of the resolved speckle sources ($V = 11.87$, $(B - V) = 0.41$) appears redder and brighter and lies closer to the CMD position of component B from my light curve and spectroscopic modeling, near the 1.6 $M_\odot$ evolutionary track. The other source is slightly bluer and fainter ($V = 12.15$, $(B - V) = 0.38$), aligning more closely with the combined light of components Aa and Ab. However, since the speckle observations do not distinguish which of the two resolved sources corresponds to the close binary A and which to component B, I cannot make a definitive association between the observed speckle components and the modeled stellar components. This result has direct implications for the prior hypothesis that S1082 is a hierarchical triple system, with component B serving as a tertiary companion to the binary A with the spectroscopic orbital period of 1185 days. The observed projected separation is inconsistent with such a compact configuration, a system with a 390 AU separation would instead have an orbital period of several thousand years. three orders of magnitude longer than the spectroscopic period. I evaluated the chance of superposition of the two binaries within M67, finding a probability of just 0.013%. If A and B form a quadruple, the absolute value of the orbital binding energy of the quadruple is higher than the average kinetic energy of stars in M67, thus being dynamically hard and stable against disruption. Taken together, these results strongly support that the binary A and the binary B are not dynamically connected in a triple configuration, but instead represent two physically associated but independently evolving binary systems, a wide, gravitationally bound pair whose mutual orbital motion is expected to occur on timescales far exceeding the current observational baseline.

5.2 O-C diagram

The $O-C$ diagram (Figure 4.3.3) reveals statistically significant timing deviations across different datasets spanning over four decades. While the recent K2 eclipse timings are consistent with the best-fit linear ephemeris, earlier observations,

particularly from Pribulla et al. (2008), Csizmadia et al. (2002), MT. Laguna data and TESS, show systematic offsets of up to ∼0.02–0.03 days.

The peak-to-peak amplitude $\Delta O - C$ is $\sim$ 63 minutes. To assess whether the observed deviations in the $O - C$ diagram could result from the light-travel-time effect (LTTE) due to orbital motion around a third body, I applied the standard formalism as outlined by V01. Given the updated masses of the eclipsing binary system – $M_{\rm Aa} \sim 1.3$ M$_\odot$ and $M_{\rm Aa} \sim 1.0$ M$_\odot$ – and assuming the third body is the BSS (binary B) with an updated mass estimate of $M_{\rm Aa} \sim 1.6$ M$_\odot$, I evaluated the minimum orbital parameters required to produce the observed peak-to-peak timing variation. For the observed $\Delta(O - C) \sim 63$ minutes (i.e., ∼0.044 days), I estimate the minimum projected semi-major axis of the eclipsing binary's orbit about the barycenter of the system $a_{o,b}$ sin i_o= 1/2 c Δ(O-C) $\sim$ 3.79 AU. This corresponds to a minimum semi-major axis of the outer orbit a_o sin i_o = $a_{o,b}$ sin i_o $(1 + M_A/M_B) \approx 9.23$ AU, and a minimum orbital period, using Kepler's third law and a total system mass $M_{\rm tot} = M_A + M_B \approx 3.9$ M$_\odot$, of $P_{\rm min} \approx 14.2$ years.

However, this interpretation is inconsistent with several independent constraints. The RV solution for component B indicates an orbital period of only $P = 1184.5 \pm$ 3.0 days (3.24 years), which is significantly shorter than the minimum period of 14.2 years derived from LTTE considerations. Furthermore, high-resolution speckle imaging reveals two resolved components at a projected separation of ∼0.4 arcseconds (or 390 AU). This implies a true semi-major axis of the outer system nearly two orders of magnitude larger than the LTTE-based estimate, with an orbital period on the order of ∼3800 years. These discrepancies indicate that the observed timing residuals in the $O - C$ diagram cannot be attributed entirely to classical LTTE caused by motion around a third body. Therefore, if component B is gravitationally bound to the eclipsing pair, the system must be hierarchical, with an outer orbital period far too long to generate detectable LTTE variations on decade timescales.

Here I explore several other potential physical mechanisms that could explain the timing discrepancies.

5.2.1 Starspots and the O'Connell Effect

The light curves of S1082 show a persistent O'Connell effect. The O'Connell effect is a brightness asymmetry between the flux maxima at the quadratures, which is indicative of large, possibly migrating starspots. Asymmetric spot coverage can shift the center of light in the system, leading to small distortions in the observed eclipse shape and timing (e.g., Watson and Dhillon, 2004; Tran et al., 2013). In such cases, the measured time of eclipse minimum may deviate from the true geometric conjunction.

This effect is more pronounced in systems with significant spot evolution on short timescales. Given the observed dispersion in the out-of-eclipse brightness and morphology in the K2 light curves, starspots are likely contributing to some of the timing scatter. However, spot-induced timing shifts are expected to vary randomly over weeks to months. They are unlikely to produce the persistent, multi-year offsets observed in the older datasets.

5.2.2 Chromospheric Activity Cycles

Another possibility is that one or both components of the binary system A undergoes magnetic activity cycles analogous to the solar cycle, with long-term variations in surface magnetic fields and associated phenomena such as chromospheric plages and enhanced spot coverage. If magnetic activity modifies the internal angular momentum distribution or induces quasi-periodic variations in the quadrupole moment of one or both stars, the orbital period can show modulations via the Applegate mechanism (Applegate and Patterson, 1987; Applegate, 1992; Völschow et al., 2018).

If the Applegate mechanism is active in S1082, the $O-C$ diagram may be tracing the history of such magnetic cycles. This explanation makes testable predictions: epochs of large O-C deviations should correlate with heightened magnetic activity, possibly observable as variations in chromospheric emission lines (e.g., Ca II H&K, Hα) or X-ray luminosity. Archival or future observations at these wavelengths could therefore help confirm or refute this scenario.

However, recent theoretical work has cast doubt on the energetic viability of the Applegate mechanism for many systems. In particular, Völschow et al. (2018) presented a detailed treatment of the angular momentum redistribution

within magnetically active stars and concluded that, for typical RS CVn-type systems, the expected amplitude of orbital period variations is often one to two orders of magnitude smaller than observed. They find the mechanism is only energetically feasible in tight post-common-envelope binaries with low-mass secondaries ($M_2 \sim 0.3$-0.36 $M_\odot$) and orbital separations $\lesssim 1$ $R_\odot$.

Given that S1082 is not a compact post-CE system and likely has more massive components, the applicability of the Applegate mechanism is questionable. While magnetic activity may still influence eclipse timing indirectly via spot evolution, it is unlikely to account for the full magnitude of the long-term residuals observed in this system.

5.2.3 Stellar Winds and Mass Loss

Mass loss via stellar winds or mass transfer between the components can lead to secular changes in the orbital period. In conservative mass transfer, the orbital period would change slowly and monotonically. However, the residuals in the $O - C$ diagram do not show a clear parabolic trend typical of mass transfer. Non-conservative mass loss, particularly through magnetic braking or episodic ejection, might induce irregular period shifts, but this mechanism is difficult to constrain without accompanying spectroscopic evidence of outflows or circumstellar material. Continued long-baseline monitoring of the system, along with multiwavelength data, would be critical for disentangling these effects.

5.3 Numerical Modeling

To complement the observational data, I performed theoretical modeling using stellar evolution and dynamical simulations. This section brings together stellar evolution calculations using MESA and dynamical simulations using FEWBODY. I start by exploring whether stable mass transfer in a close binary can explain the properties of S1082 A, and then move on to test whether dynamical encounters involving binaries and triples could produce a similar outcome. In cases where dynamical interactions lead to compact binaries, I use MESA again to follow the subsequent tidal evolution and assess whether the observed orbital period can be reached.

5.3.1 MESA Mass Transfer Simulations

I performed simulations to test stable Case A mass transfer as the formation mechanism of binary A. I employed the stellar evolution code Modules for Experiments in Stellar Astrophysics (MESA Paxton et al., 2011, 2013, 2015, 2018, 2019; Jermyn et al., 2023) to model a grid of binary evolution tracks. All simulations assumed solar metallicity ($Z = 0.02$) and neglected stellar winds. Both conservative and non-conservative mass transfer prescriptions were tested. The total binary mass was fixed at 2.3 $M_\odot$ to reflect the observed mass of S1082 A. I explored a wide range of initial donor masses ($M_{1,\mathrm{init}} = 1.15$–$1.60$ $M_\odot$ in steps of 0.01 $M_\odot$), with the secondary mass adjusted to maintain the total mass. Initial orbital periods ranged from 0.5 to 1.1 days in 0.1-day steps.

Each model was categorized according to its evolutionary outcome. In some, the donor star evolved off the main sequence without filling its Roche lobe, thereby failing to trigger mass transfer. In others, mass transfer initiated but quickly led to a contact binary configuration in which the accretor also overfilled its Roche lobe. In my MESA framework, such configurations terminate the calculation. While my treatment treats contact as an endpoint, in reality some contact binaries may return to detached or semi-detached configurations once the accretor regains thermal equilibrium and contracts (Henneco et al., 2024), so my models may under represent certain possible evolutionary pathways. Here I focus on the remaining subset of models that experienced two episodes of mass transfer: the first while the donor was on the main sequence, and the second after core hydrogen exhaustion. I searched for configurations in which the initial mass transfer episode occurred within the first 4 Gyr, consistent with the age of M67.

After modeling 624 binary configurations, none reproduced the present-day configuration of S1082 A. The primary inconsistency lies in the evolutionary state of the current secondary star, which appears on the slightly evolved portion of the main sequence in the CMD, consistent with ongoing hydrogen burning and moderate helium enrichment. In contrast, all models predict that the post-mass-transfer donor would be a thermally contracting proto-white dwarf, significantly underluminous relative to the current position of star Ab in the CMD (e.g., Figure 5.3.1).

This discrepancy arises because stable mass transfer strips the donor's hydrogen-

rich envelope, halting core hydrogen fusion. The resulting remnant cools and fades, becoming progressively redder. Such behavior is a well-established outcome of standard binary evolution theory (e.g., Nelson and Eggleton 2001; Lu et al. 2010). Even when mass transfer begins relatively early on the MS, my models tend to either strip too much mass (collapsing H-burning entirely) or evolve toward contact, neither of which match the observed state. Producing a $\sim$1.0 $M_\odot$ MS secondary while halting mass transfer during the later stages of H burning remains an unsolved problem in my models.

The representative example from my grid of conservative mass transfer models, with an initial primary of 1.23 $M_\odot$, a secondary of 1.07 $M_\odot$, and an initial period of 0.95 days, illustrates the general behavior (see Figure 5.3.1). The first episode of mass transfer occurs after 4 Gyr, so at this age both components remain on their detached evolutionary tracks. At 4 Gyr, the donor (orange track) remains on the subgiant branch and happens to lie near the CMD position of S1082 Ab, but this is pre–mass-transfer. By 4.87 Gyr (marked with diamond symbols), mass transfer has occurred, the donor has left the subgiant branch and evolved toward lower luminosity, while the accretor (blue track) has gained mass and migrated toward the blue straggler region, near the current position of S1082 Aa. However, the donor's post-transfer position is far too faint to match Ab. More generally, in my models the donor invariably evolves off the main sequence as MT begins, while the accretor tends to become too massive, often exceeding 1.6 $M_\odot$, which is inconsistent with the revised dynamical mass.

These findings hold even when relaxing constraints on the present-day dynamical masses and instead focusing solely on matching the CMD positions of the two stars. No combination of binary parameters tested could simultaneously reproduce the observed luminosity and temperature of both components at 4 Gyr. In particular, the position of the current secondary (Ab) in the CMD is incompatible with that of a post–mass-transfer remnant. In every simulation, the donor ends as a stripped, underluminous object, whereas Ab appears consistent with a main-sequence star.

This discrepancy leaves two broad possibilities: either an atypical form of mass transfer, potentially episodic, prematurely truncated, or occurring under conditions that avoid extreme mass-ratio reversal, or the current secondary is a main-sequence star that was dynamically inserted into the system after the original donor was lost. The latter explanation is supported by my dynamical simulations (Section

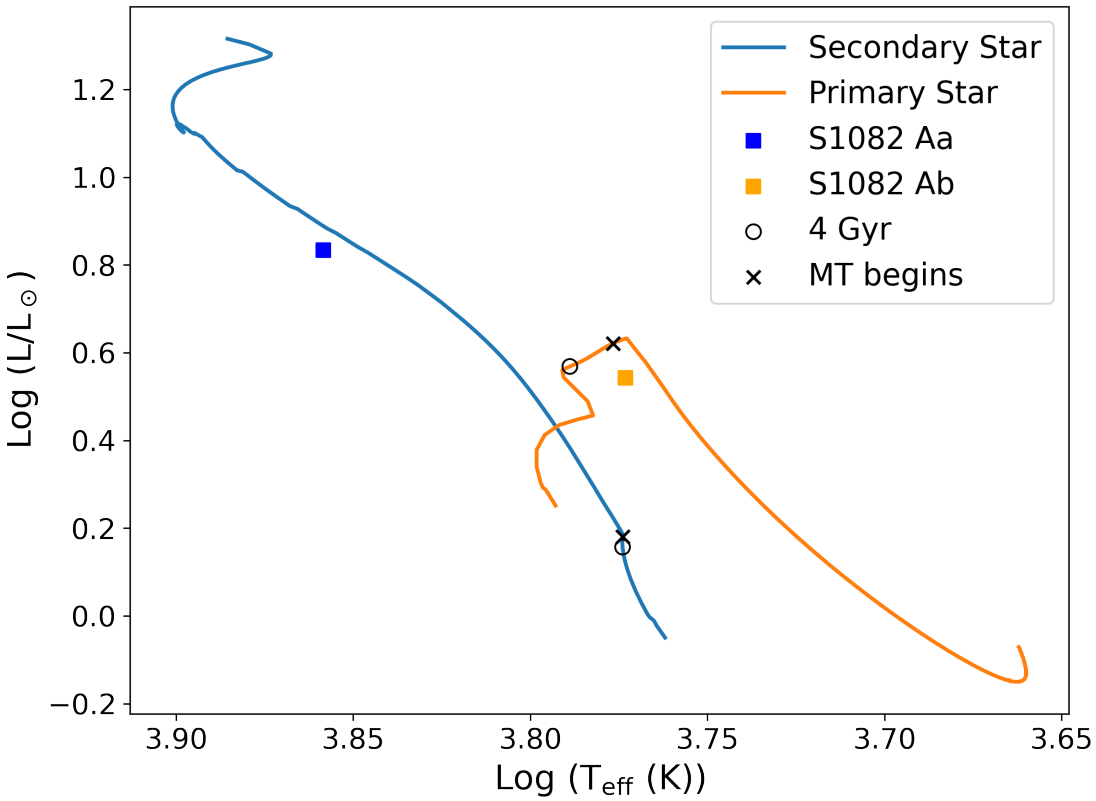

Figure 5.3.1: HR diagram showing the evolution of a representative conservative MESA mass transfer model, with initial masses of 1.23 $M_\odot$ (donor, orange) and 1.07 $M_\odot$ (accretor, blue), and initial orbital period of 0.95 days. Filled squares mark the observed positions of S1082 Aa and Ab. Circles show the model positions at 4 Gyr, crosses indicate when mass transfer begins, and diamonds mark the positions at 4.87 Gyr after mass transfer has altered both stars' evolution.

5.3.2), which show that BSS binaries like S1082 A can plausibly result from a combination of mass transfer and subsequent dynamical exchanges, with the present secondary replacing the original donor.

5.3.2 Numerical scattering simulations and tidal circularization

To explore the possibility that S1082 A formed as a result of a dynamical interaction, I performed numerical scattering simulations using FEWBODY (Fregeau et al., 2004), a toolkit designed for simulating gravitational encounters involving small-N stellar systems. While the previous section demonstrated that isolated binary evolution fails to explain the observed configuration of S1082 A, dynamical processes in a dense cluster like M67 could provide an alternative formation pathway and significantly change the picture. I modeled two different types of stellar encounters that could plausibly produce the observed system: binary-triple (2+3) and binary-single (2+1) interactions.

5.3.2.1 Binary-Triple (2+3) interactions

As mentioned in Section 4.2, the speckle imaging analysis supports the interpretation of S1082 as a hierarchical quadruple system composed of a close binary (S1082 A) and a wider binary (S1082 B). Under this assumption, I first evaluated the energetic plausibility of this configuration. I estimated the orbital binding energy of the proposed quadruple system by treating S1082 A and B as two bound subsystems orbiting a common center of mass. The computed energy, $E\_\mathrm{orb} \approx 9.15 \times 10^{36}$ J, significantly exceeds the average kinetic energy of stars in M67 ($E\_\mathrm{kin} \approx 3.46 \times 10^{35}$ J), suggesting the system is dynamically "hard" and stable against disruption. With a projected separation of 390 AU (assuming a circular orbit) this corresponds to a semi-major axis of $\tilde{0}.0019$ pc, while typical inter-particle distances in M67's core are $\sim$0.2 pc. This implies that a stable quadruple configuration with this separation is dynamically plausible in the cluster.

Triple star systems are now recognized as dynamically important components in star cluster environments, with interactions involving triples occurring as frequently as, or even more frequently than, those involving binaries or single stars, particularly in low-mass clusters like M67 (Leigh and Geller, 2013). Higher-

order multiples enhance the cross-section for dynamical encounters, increasing the likelihood of complex outcomes such as collisions or the formation of binaries (Leigh and Geller, 2012). The relevance of 2+3 encounters in M67 is supported by encounter timescale estimates. Using the formalism in Appendix A of Leigh and Sills (2011), and assuming a binary fraction of 0.5 (Fan et al., 1996) and a $f_b/f_t = 0.1$ (Leigh and Sills, 2011), I find that such interactions occur on timescales of $\sim 2 \times 10^7$ years, which is much shorter than the cluster age, and well within the typical BSS lifetime (Tian et al., 2006).

Motivated by this, I simulated 80,000 binary-triple encounters. In this setup, the incoming binary contained a BSS (1.3 $M_\odot$, 1.67 $R_\odot$) and a white dwarf (0.36 $M_\odot$, 0.05 $R_\odot$) formed through a previous episode of Case B mass transfer (Paczyński, 1971). I focus on Case B specifically because it typically leads to stable mass transfer (Soberman et al., 1997; Ge et al., 2020; Temmink et al., 2023), which avoids the complexities and uncertainties associated with common-envelope evolution. Moreover, such stable interactions generally produce binaries with wider separations (e.g., Soberman et al. (1997)), increasing the cross-section for subsequent dynamical encounters. This makes them more likely to participate in interactions like the one modeled here. The target hierarchical triple was composed of a BSS (1.4 $M_\odot$, 1.8 $R_\odot$) and a WD (0.35 $M_\odot$, 0.05 $R_\odot$) in a 3 AU, $e = 0.6$ inner binary, with a 1.0 $M_\odot$ MS star (1.77 $R_\odot$) in a 390 AU, $e = 0.3$ outer orbit. These configurations satisfy the dynamical stability criterion of Mardling and Aarseth (2001). The initial eccentricity of the incoming binary was set to zero.

In these simulations, the stellar masses and radii were fixed for all runs. The binary initially designated as object 1 contains stars of masses 1.3 $M_\odot$ and 0.36 $M_\odot$, and radii 1.67 $R_\odot$ and 0.05 $R_\odot$, respectively. The more massive star represents the BSS in S1082 A. The 0.36 $M_\odot$ star represents a WD remnant of an earlier episode of stable mass transfer. The hierarchical triple (object 0) contains an inner binary composed of 1.4 $M_\odot$ and 0.35 $M_\odot$ stars, with radii of 1.8 $R_\odot$ and 0.05 $R_\odot$ (representing the BSS and its subluminous companion in S1082 B), and a MS outer tertiary companion of 1.0 $M_\odot$ and radius 1.77 $R_\odot$. The radius of the MS star in these models resembles the radius of the MS star in S1082 A. The masses of the WDs were selected to allow tracking of the components post-encounter. All mass transfer events and internal stellar evolution were assumed to occur

before the encounter, and thus stellar properties remained constant during the simulations. Mergers were included as possible outcomes in all runs, following FEWBODY's "sticky star" prescription (Fregeau et al., 2004). In this approach, stars are treated as rigid spheres with radii equal to their stellar radii, merging upon contact with no mass loss and conserving linear momentum. For MS-MS collisions, the expansion factor $f_{\rm exp}$ is set to 1, so the merger radius is simply $R_{\rm merger} = R_1 + R_2$. While mergers were not the primary focus of this work, they were naturally recorded in the simulation outcomes.

I varied the initial semi-major axis of the incoming binary (a_1), sampling values uniformly between 0.05 AU and 4.0 AU in steps of 0.05 AU. The other orbital elements were kept fixed across all simulations. Each combination of orbital parameters defined a set of 1,000 realizations, or "seeds", in which the impact parameter was uniformly sampled between 0 and $b\_\max = 5 \times (a\_0 + a\_1)$, in units of $a_0 + a_1$, where $b_{\max}$ was chosen similar to that of Fregeau et al. (2004). The velocity at infinity v_∞ was drawn from a Maxwellian distribution with a velocity dispersion of 0.59 km s^{-1}, consistent with M67's internal kinematics (Geller et al., 2015a). The semi-major axis of the incoming binary was varied from 0.05 to 4.0 AU in steps of 0.05 AU.

I searched specifically for outcomes matching the hierarchical structure [[0 1] [2 3]] 4, corresponding to a hierarchical quadruple system composed of two post-encounter binaries ([0,1] and [2,3]) and a single star ejected from the system (star 4). In this nomenclature, stars 0 and 1, with masses of 1.4 and 0.35 $M_\odot$ are the components analogous to the BSS and presumed WD in S1082 B, while stars 2 and 3 (1.0 $M_\odot$ and 1.3 $M_\odot$) represents the MS and BSS in S1082 A.

Among the 80,000 simulations, 227 ended in this desired configuration, corresponding to a success rate of ∼0.28%. For each successful outcome, I extracted the final orbital elements of the post-encounter (2,3) binary and the outer orbit between the two binaries.

The distribution of final orbital periods for the (2,3) binaries showed a clear dependence on the initial semi-major axis of the incoming binary. As shown in Figure 5.3.2, a sub-linear power-law relation, $a\_\text{initial} \propto P^{0.513}\_\text{final, binary}$, was observed, indicating that tighter initial binaries tend to produce shorter-period remnants. Close binaries with orbital periods near the observed 1.068-day period

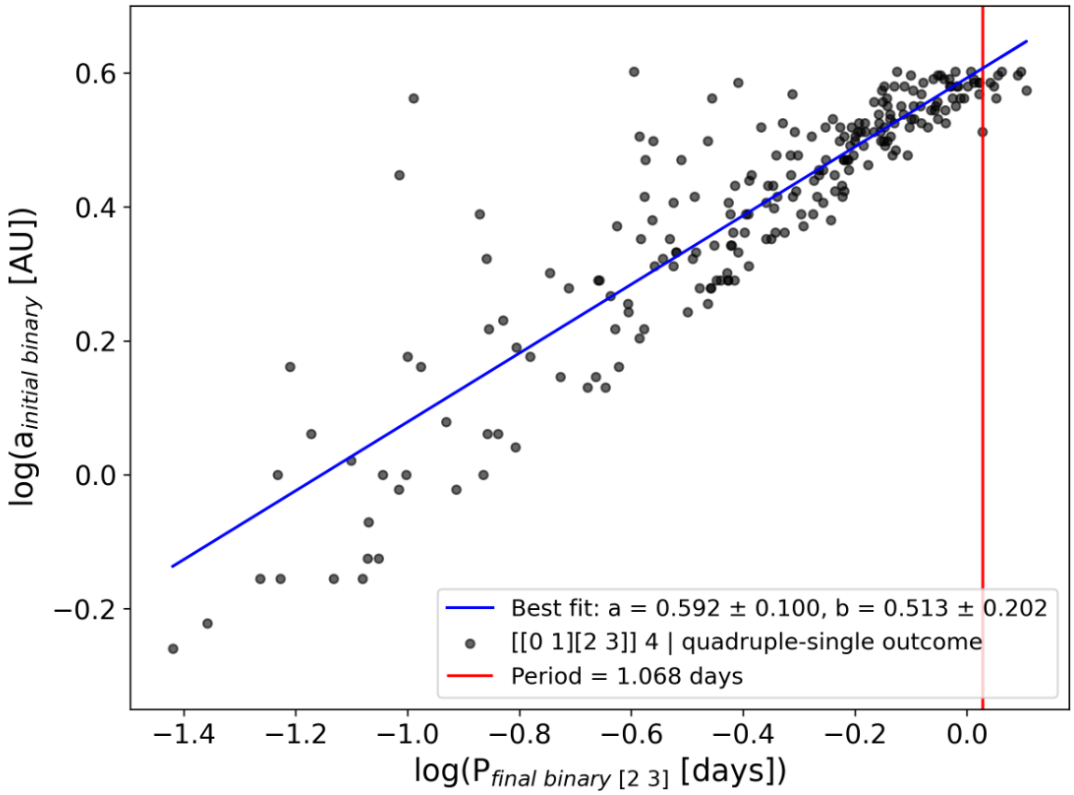

Figure 5.3.2: Relation between the final orbital period of the close binary ([2 3]) and the initial semi-major axis of the incoming binary (a_1) in 2+3 encounters that resulted in a quadruple-single configuration. The best-fitting linear relation is shown in blue. The red vertical line marks the location of the observed orbital period of the close binary in S1082 (1.068 days).

of S1082 A were indeed produced.

However, the orbital periods between the two binaries (the full quadruple) were consistently in the 500–5000 day range, peaking around 10^3 days (see Figure 5.3.3). This is more than two orders of magnitude shorter than the orbital period corresponding to the observed 390 AU separation ($\sim 10^6$ days), and thus inconsistent with the real system. Moreover, I estimated the typical interaction timescale for such a wide quadruple system in M67 to be only 7.5×10^6 years, suggesting that even if such systems form, they are unlikely to survive over Gyr timescales. These findings imply that while my 2+3 encounters can create systems with the internal architecture of S1082, they cannot simultaneously reproduce its wide separation.

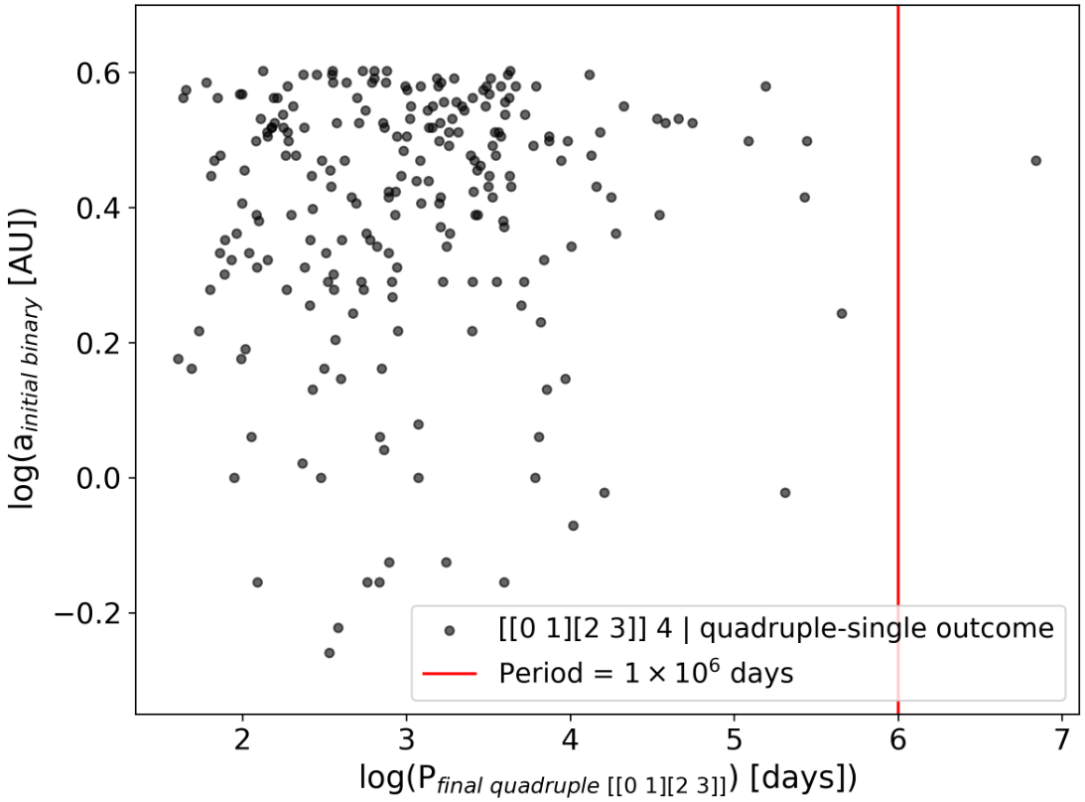

Figure 5.3.3: Relation between the final orbital period of the outer quadruple system ([[0 1][2 3]]) and the initial semi-major axis of the incoming binary (a_1) in 2+3 encounters that resulted in a quadruple-single configuration. The red vertical line indicates a period of 1×10^6 days, which is close to the orbital timescale inferred from the projected separation of the resolved components of S1082 (390 AU).

5.3.2.2 Binary-Single (2+1) interactions

I next considered an alternative scenario in which S1082 A formed through a binary-single (2+1) encounter, with the assumption that the close binary S1082 A is an isolated system. In this setup, a close binary containing a BSS and a WD (again formed through earlier Case B mass transfer) interacts with a single 1.0 $M_\odot$ MS star. If the WD is ejected and the MS star captured, this can yield a BSS–MS binary without requiring a subsequent mass transfer phase.

To explore this, I performed 59 independent FEWBODY simulations of 1,000 seeds each, for a total of 59,000 2+1 encounters. The initial binary consisted of a BSS (1.3 $M_\odot$, 1.67 $R_\odot$) and a WD (0.36 $M_\odot$, 0.01 $R_\odot$). The incoming single was a 1.0 $M_\odot$ MS star. As in the 2+3 simulations, the impact parameter b and the velocity at infinity v_∞ were drawn from a uniform distribution and a Maxwellian distribution corresponding to the kinematic environment of M67, respectively. All runs used fixed stellar masses and radii, and assumed circular orbits, as perhaps are created during the earlier mass transfer. Mergers were also tracked in these runs using the same FEWBODY prescription, with $f_{\rm exp} = 1$. The initial semi-major axis of the binary (A1) was varied from 0.05 to 3.0 AU in steps of 0.05 AU. This design allowed us to systematically probe the sensitivity of the encounter outcomes to the initial binary separation.

Each set yielded a dominant number of binary-single outcomes ([0 1] 2), with 38,032 producing this configuration. This outcome corresponded to a BSS-MS binary system and a single WD. The distribution of the final orbital periods and pericenter distances of the simulations that ended in the wanted outcome are shown in Figure 5.3.4. I found that for small values of A1 (0.1 AU), the simulations were strongly dominated by merger events, with very few binary-single outcomes. However, for A1 values above 1 AU, the desired outcome stabilized at $\sim$70% frequency across seeds. Among these binaries, 737 had orbital periods $<$100 days and 173 had pericenter distances $<$0.05 AU, close to the semi-major axis of S1082 A ($\sim$0.02 AU), representing a fraction of $\sim$ 0.3% of the total simulations. Furthermore, only four systems achieved orbital periods $<$10 days, with the shortest at 5.67 days. Thus, while the pericenter distances became compact, the orbital periods remained significantly longer than the observed value.

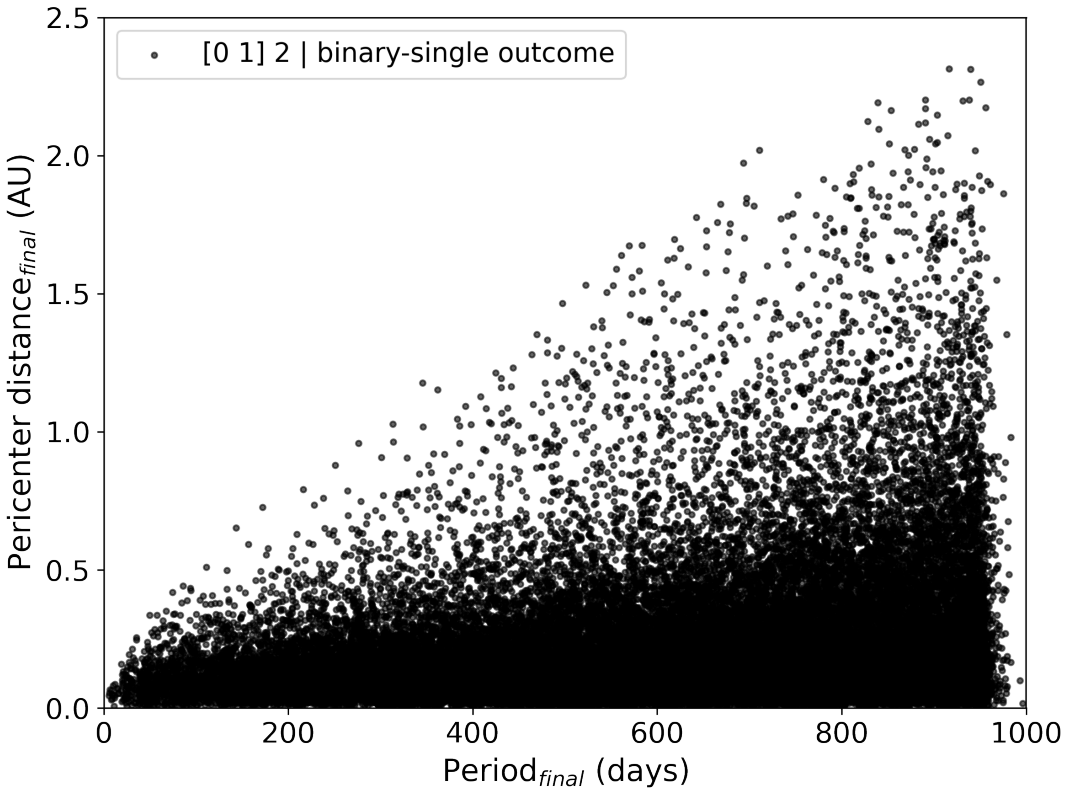

Figure 5.3.4: Distribution of the final orbital periods and pericenter distances for all FEWBODY simulations that produced the desired [0 1] 2 binary-single outcome.

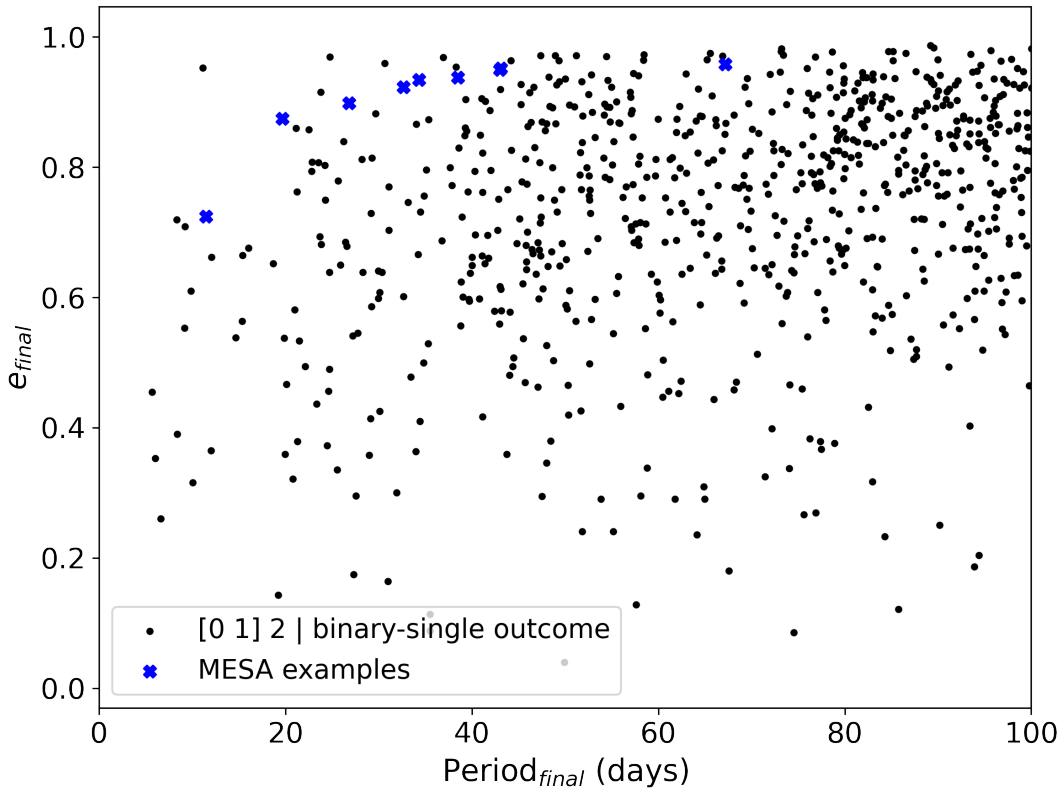

Figure 5.3.5: Final orbital eccentricity vs. period for all FEWBODY simulations that produced the desired [0 1] 2 binary-single outcome with $P_{\rm final} < 100$ days. Blue crosses show the subset of systems selected for MESA tidal circularization modeling.

5.3.2.3 Tidal Circularization with MESA

Given the pericenter compactness of several binaries formed in 2+1 interactions, I explored whether tidal circularization could reduce their periods to match S1082 A. To do this, I selected nine post-encounter binaries with final periods <100 days (blue crosses at Figure 5.3.5) and evolved them using MESA, incorporating tidal synchronization and circularization.

Each system was initialized using the final orbital period (P_initial) and eccentricity (e_initial) from FEWBODY. The primary was modeled as a 1.3 $M_\odot$ star, and the secondary as 1.2 $M_\odot$ star, higher than the observed 1.0 $M_\odot$ value for Ab, to reflect its anomalously large radius ($\sim$1.77 $R_\odot$), which would enhance tidal effects. The systems were evolved to 4 Gyr.

Final periods ranged from 1.215 to 3.76 days (see Table 5.3.1), with the shortest (Run 38) approaching the observed 1.068-day period of S1082 A. Several runs

Table 5.3.1: Initial orbital parameters from FEWBODY simulations used as input for MESA tidal circularization models, and the resulting final orbital period at 4 Gyr.

P_{initial} (days)	e_{initial}	P_{final} (days)
11.45	0.724	3.76
19.67	0.875	2.224
26.82	0.898	2.273
32.64	0.923	1.849
34.30	0.935	1.515
38.46	0.938	1.591
43.00	0.950	1.290
43.12	0.952	1.215
67.18	0.958	1.570

terminated with final periods within 15% of the observed value. These results represent more than an order-of-magnitude orbital decay from the original periods (11–67 days), highlighting the efficiency of tidal circularization. The distribution of eccentricity versus final period is shown in Figure 5.3.5, and the initial and final periods are listed in Table 5.3.1.

While none of the runs reproduced S1082 A's period, they show that tidal circularization following a 2+1 interaction is a viable mechanism for producing close, detached BSS–MS binaries. Modest changes in initial conditions, like slightly shorter separations or more extreme eccentricities, could plausibly yield the observed period, especially when accounting for uncertainties in tidal dissipation physics. Furthermore, MESA models treat the BSS as a canonical MS star, neglecting potentially critical structural and rotational peculiarities that would affect tidal evolution. Similarly, the larger-than-expected radius of the secondary implies unusually deep convection, potentially enhancing tidal dissipation.

Thus, although the present simulations fall slightly short of the precise configuration of S1082 A, they support a two-step formation pathway: BSS formation via mass transfer, followed by a dynamical exchange and tidal circularization, potentially involving enhanced structural dissipation mechanisms not yet implemented in current models.

Additionally, my simulations suggest that while a bound quadruple configuration composed of two binaries is not physically forbidden, it is an extremely rare outcome under the dynamical conditions expected in M67. The required orbital

configuration of a 1.07-day BSS–MS binary and a 1000+ day BSS–WD binary bound in a orbit of $\sim 10^6$ days, occupies a narrow and likely unstable region of parameter space. In contrast, the formation of S1082 A as an independent binary product of a 2+1 encounter, followed by tidal circularization, is a more probable scenario. Therefore, the simulations support the interpretation that S1082 A is most plausibly the outcome of a dynamical exchange involving a BSS–WD progenitor and a single MS star, evolving independently of S1082 B. The physical connection between A and B may reflect a later dynamical pairing rather than a shared formation history.

In addition to the two distinct scenarios modeled in this study, a hybrid dynamical scenario can also be possible. In this picture, the present-day binary BSS in S1082 A first forms through a mass-transfer episode in a progenitor binary composed of two MS stars. The most massive star evolves and transfers mass to its companion, producing a BSS and leaving behind a WD. A subsequent 2+1 encounter involving this BSS–WD binary and an incoming MS star can then eject the WD, leaving behind a compact BSS–MS binary similar to the present-day S1082 A. Because of its short orbital period, such a binary would behave dynamically as a single 'hard' object in future encounters. The formation of the present-day quadruple could then proceed in a later 2+3 encounter, where the BSS–MS binary interacts with a hierarchical triple. In this scenario, the triple might consist of an inner BSS–WD binary and a more distant MS tertiary. During the encounter, the tertiary MS star is likely to be ejected, and the outcome would be a bound wide quadruple comprised of the 1-day BSS–MS binary (S1082 A) and the ∼1000-day BSS-WD binary (S1082 B). The observed projected separation of 390 AU between S1082 A and B would require an outcome in which the two binaries are left bound but at relatively large separation, which is energetically possible provided that the ejected tertiary star carries away sufficient binding energy.

A rough estimate of the timescale between a 2+3 encounter in the core of M67 gives $\sim 2.2 \times 10^7$ yr, which is short compared to the cluster age and therefore not implausible. While I have not modeled this scenario directly, its qualitative plausibility could show a pathway in which both the formation of S1082 A and the present-day quadruple configuration could be linked by sequential dynamical events. Quantifying the likelihood of this channel would require targeted simulations that systematically explore the energetics and stability of such 2+3 outcomes.

Despite the promising results of my simulations, it is important to recognize key limitations in my models. The initial conditions for the dynamical encounters were chosen based on the currently observed separations and orbital parameters of the components, particularly the close nature of S1082 A and the wide projected separation of 390 AU between A and B. However, during dynamical interactions, especially those involving exchanges or reconfigurations of multiple stars, the orbital parameters of subsystems can be substantially altered. The final architecture of the system may not directly reflect the pre-encounter orbital parameters. In the case of 2+1 encounters, sampling tighter binaries could increase the probability of merger events, reducing the likelihood of producing stable binaries resembling S1082 A. On the other hand, increasing the initial separations and including more eccentric orbits might enhance the formation of the desired hierarchical outcomes. However, such broadening also reduces the likelihood of producing post-encounter binaries as compact as S1082 A.

Future modeling efforts should therefore consider a more flexible approach. Rather than constraining the initial binary parameters to the observed parameters, simulations could allow broader variation in initial periods and eccentricities.

Chapter 6

Conclusion

S1082 is a remarkable stellar system in the open cluster M67. It is likely a quadruple system comprising a close eclipsing binary (S1082 A; period 1.07 days) and a wider binary (S1082 B; 1185 days), with both sub-systems hosting BSS stars. Historically the masses and radii of the components of this system have been puzzling. In this study, I have updated the physical measurements of these stars, and tried to reconstruct the formation history of the system.

I combined high-precision photometry from the K2 and TESS missions with older photometric observations, new RV data, and speckle imaging to refine the orbital and physical parameters of the system. The RV data yielded a revised orbital solution for the close binary A, while the speckle observations confirmed the presence of two sources separated in projection by 0.463 arcseconds. The mass of the primary and secondary in the eclipsing binary were determined to be 1.3 $M_{\odot}$ and 1.0 $M_{\odot}$, respectively, notably lower than what previous studies reported. The projected separation between the A and B subsystems is 390 AU. This makes it unlikely for the 1185-day spectroscopic period of component B to correspond to the wide orbit of a triple system, and therefore supports the scenario of S1082 being a quadruple system comprising two binaries.

Collectively, the LC parameters support a more coherent evolutionary scenario for the system, one that reduces the tension with M67 cluster constraints and suggests that extreme dynamical histories, such as multi-star collisions, may no longer be necessary to explain S1082's current state

To evaluate different formation scenarios, I performed stellar evolution simulations

using MESA and dynamical scattering experiments using FEWBODY. The MESA simulations show that mass transfer between two main sequence stars cannot reproduce the observed configuration of the close binary A, particularly due to the evolutionary status of the current secondary, which remains on the MS and is inconsistent with the expected properties of a post-mass-transfer donor.

I then explored dynamical formation channels, including 2+3 and 2+1 encounters. My simulations show that while the formation of a hierarchical quadruple system through a 2+3 encounter is dynamically possible, it does not typically yield binaries with the short periods and compact configurations observed in S1082 A, within the parameter space I explored. In contrast, 2+1 encounters frequently produce binary-single outcomes where a MS star replaces a white dwarf companion. Among the simulated encounters, a subset produced binaries with short pericenter distances and moderately short periods. I followed these systems with tidal evolution simulations in MESA. Although none reproduced the exact orbital period of S1082 A, a portion evolved to within 15 percent of the observed value. These results suggest that a 2+1 encounter followed by tidal circularization may be the most likely formation scenario.

My findings support a scenario in which the BSSs in S1082 were formed first, followed by a subsequent dynamical interaction that assembled the current configuration of the close binary. S1082 A most plausibly formed through a dynamical exchange involving a BSS–WD progenitor and a MS intruder, evolving independently from S1082 B. If A and B are currently gravitationally bound, their association likely occurred after their individual formation through subsequent dynamical processes.

My analysis of S1082 shows that the formation of close blue straggler binaries in clusters may not be fully explained through isolated mass transfer alone, but also through later dynamical processes that reshape their parameters. My study shows how combining detailed observational constraints with tailored numerical modeling enables the reconstruction of such complex formation pathways. The approach developed here for S1082 provides a useful methodology for analyzing other multiple systems containing blue stragglers. Applying this method across a larger sample could help assess the relative roles of mass transfer and dynamical interactions in blue straggler formation. Further progress will require improved tidal evolution prescriptions and a broader exploration of the parameter space.

Bibliography

Andronov, N., Pinsonneault, M. H., and Terndrup, D. M. (2006). Mergers of Close Primordial Binaries. , 646(2):1160–1178.

Applegate, J. H. (1992). A Mechanism for Orbital Period Modulation in Close Binaries. , 385:621.

Applegate, J. H. and Patterson, J. (1987). Magnetic Activity, Tides, and Orbital Period Changes in Close Binaries. , 322:L99.

Balaguer-Núñez, L., Galadí-Enríquez, D., and Jordi, C. (2007). uvby - H_β CCD photometry and membership segregation of the open cluster NGC 2682 (M 67). , 470(2):585–596.

Belloni, T., Verbunt, F., and Mathieu, R. D. (1998). X-rays from old open clusters: M 67 and NGC 188. , 339:431–439.

Belloni, T., Verbunt, F., and Schmitt, J. H. M. M. (1993). ROSAT detection of stellar X-ray sources in the old open cluster M 67. , 269:175–180.

Borucki, W. J., Koch, D., Basri, G., Batalha, N., Brown, T., Caldwell, D., Caldwell, J., Christensen-Dalsgaard, J., Cochran, W. D., DeVore, E., Dunham, E. W., Dupree, A. K., Gautier, T. N., Geary, J. C., Gilliland, R., Gould, A., Howell, S. B., Jenkins, J. M., Kondo, Y., Latham, D. W., Marcy, G. W., Meibom, S., Kjeldsen, H., Lissauer, J. J., Monet, D. G., Morrison, D., Sasselov, D., Tarter, J., Boss, A., Brownlee, D., Owen, T., Buzasi, D., Charbonneau, D., Doyle, L., Fortney, J., Ford, E. B., Holman, M. J., Seager, S., Steffen, J. H., Welsh, W. F., Rowe, J., Anderson, H., Buchhave, L., Ciardi, D., Walkowicz, L., Sherry, W., Horch, E., Isaacson, H., Everett, M. E., Fischer, D., Torres, G., Johnson, J. A., Endl, M., MacQueen, P., Bryson, S. T., Dotson, J., Haas, M., Kolodziejczak, J., Van Cleve, J., Chandrasekaran, H., Twicken, J. D., Quintana, E. V., Clarke, B. D., Allen, C., Li, J., Wu, H., Tenenbaum, P., Verner, E., Bruhweiler, F., Barnes, J., and Prsa, A. (2010). Kepler Planet-Detection Mission: Introduction and First Results. *Science*, 327(5968):977.

Budding, E. and Zeilik, M. (1987). An Analysis of the Light Curves of Short-Period RS Canum Venaticorum Stars: Starspots and Fundamental Properties. , 319:827.

Cao, L. and Stassun, K. G. (2025). The Relationship of Stellar Radius Inflation to Rotation and Magnetic Starspots at 10–670 Myr. , 988(1):L1.

Castelli, F., Gratton, R. G., and Kurucz, R. L. (1997). Notes on the convection in the ATLAS9 model atmospheres. , 318:841–869.

Chen, X. and Han, Z. (2008). Mass transfer from a giant star to a main-sequence companion and its contribution to long-orbital-period blue stragglers. , 387(4):1416–1430.

Choi, J., Dotter, A., Conroy, C., Cantiello, M., Paxton, B., and Johnson, B. D. (2016). Mesa Isochrones and Stellar Tracks (MIST). I. Solar-scaled Models. , 823(2):102.

Clark, C. A., van Belle, G. T., Horch, E. P., Trilling, D. E., Hartman, Z. D., Collins, M., von Braun, K., and Gehring, J. (2020). The optomechanical design of the Quad-camera Wavefront-sensing Six-channel Speckle Interferometer (QWSSI). In Tuthill, P. G., Mérand, A., and Sallum, S., editors, *Optical and Infrared Interferometry and Imaging VII*, volume 11446 of *Society of Photo-Optical Instrumentation Engineers (SPIE) Conference Series*, page 114462A.

Colton, N. M., Horch, E. P., Everett, M. E., Howell, S. B., Davidson, Jr., J. W., Baptista, B. J., and Casetti-Dinescu, D. I. (2021). Identifying Bound Stellar Companions to Kepler Exoplanet Host Stars Using Speckle Imaging. , 161(1):21.

Csizmadia, S., Zhou, A. Y., Konyves, V., Varga, Z., and Sandor, Z. (2002). Times of Minima of Eclipsing Binaries. *Information Bulletin on Variable Stars*, 5230:1.

Deeg, H. J. (2020). A Modified Kwee–Van Woerden Method for Eclipse Minimum Timing with Reliable Error Estimates. *Galaxies*, 9(1):1.

Dotter, A. (2016). MESA Isochrones and Stellar Tracks (MIST) 0: Methods for the Construction of Stellar Isochrones. , 222(1):8.

Eggleton, P. P. (1983). Aproximations to the radii of Roche lobes. , 268:368–369.

Fan, X., Burstein, D., Chen, J. S., Zhu, J., Jiang, Z., Wu, H., Yan, H., Zheng, Z., Zhou, X., Fang, L. Z., Chen, F., Deng, Z., Chu, Y., Hester, J. J., Windhorst, R. A., Li, Y., Lu, P., Sun, W. H., Chen, W. P., Tsay, W. S., Chiueh, T. H., Chou, C. K., Ko, C. M., Lin, T. C., Guo, H. J., and Byun, Y. I. (1996). Deep Wide-Field Spectrophotometry of the Open Cluster M67. , 112:628.

Flower, P. J. (1996). Transformations from Theoretical Hertzsprung-Russell Diagrams to Color-Magnitude Diagrams: Effective Temperatures, B-V Colors, and Bolometric Corrections. , 469:355.

Foreman-Mackey, D., Hogg, D. W., Lang, D., and Goodman, J. (2013). emcee: The MCMC Hammer. , 125(925):306.

Fregeau, J. M., Cheung, P., Portegies Zwart, S. F., and Rasio, F. A. (2004). Stellar collisions during binary-binary and binary-single star interactions. , 352(1):1–19.

Ge, H., Webbink, R. F., Chen, X., and Han, Z. (2020). Adiabatic Mass Loss in Binary Stars. III. From the Base of the Red Giant Branch to the Tip of the Asymptotic Giant Branch. , 899(2):132.

Geller, A. M., Latham, D. W., and Mathieu, R. D. (2015a). Stellar Radial Velocities in the Old Open Cluster M67 (NGC 2682). I. Memberships, Binaries, and Kinematics. , 150(3):97.

Geller, A. M., Latham, D. W., and Mathieu, R. D. (2015b). VizieR Online Data Catalog: Radial velocities in M67. I. 1278 candidate members (Geller+, 2015). VizieR On-line Data Catalog: J/AJ/150/97. Originally published in: 2015AJ....150...97G.

Goranskij, V. P., Kusakin, A. V., Mironov, A. V., Moshkaljov, V. G., and Pastukhova, E. N. (1992). New bright eclipsing binary in messier 67. *Astronomical and Astrophysical Transactions*, 2(3):201–208.

Henneco, J., Schneider, F. R. N., and Laplace, E. (2024). Contact tracing of binary stars: Pathways to stellar mergers. , 682:A169.

Hills, J. G. and Day, C. A. (1976). Stellar Collisions in Globular Clusters. , 17:87.

Horch, E. P., Broderick, K. G., Casetti-Dinescu, D. I., Henry, T. J., Fekel, F. C., Muterspaugh, M. W., Willmarth, D. W., Winters, J. G., van Belle, G. T., Clark, C. A., and Everett, M. E. (2021). Observations with the Differential Speckle Survey Instrument. X. Preliminary Orbits of K-dwarf Binaries and Other Stars. , 161(6):295.

Horch, E. P., Veillette, D. R., Baena Gallé, R., Shah, S. C., O'Rielly, G. V., and van Altena, W. F. (2009). Observations of Binary Stars with the Differential Speckle Survey Instrument. I. Instrument Description and First Results. , 137(6):5057–5067.

Howell, S. B. (1989). Two-Dimensional Aperture Photometry: Signal-to-Noise Ratio of Point-Source Observations and Optimal Data-Extraction Techniques. , 101:616.

Howell, S. B., Sobeck, C., Haas, M., Still, M., Barclay, T., Mullally, F., Troeltzsch, J., Aigrain, S., Bryson, S. T., Caldwell, D., Chaplin, W. J., Cochran, W. D., Huber, D., Marcy, G. W., Miglio, A., Najita, J. R., Smith, M., Twicken, J. D., and Fortney, J. J. (2014). The K2 Mission: Characterization and Early Results. , 126(938):398.

Hut, P., McMillan, S., Goodman, J., Mateo, M., Phinney, E. S., Pryor, C., Richer, H. B., Verbunt, F., and Weinberg, M. (1992). Binaries in Globular Clusters. , 104:981.

Jadhav, V. V., Sindhu, N., and Subramaniam, A. (2019). UVIT Open Cluster Study. II. Detection of Extremely Low Mass White Dwarfs and Post-Mass Transfer Binaries in M67. , 886(1):13.

Jermyn, A. S., Bauer, E. B., Schwab, J., Farmer, R., Ball, W. H., Bellinger, E. P., Dotter, A., Joyce, M., Marchant, P., Mombarg, J. S. G., Wolf, W. M., Sunny Wong, T. L., Cinquegrana, G. C., Farrell, E., Smolec, R., Thoul, A., Cantiello, M., Herwig, F., Toloza, O., Bildsten, L., Townsend, R. H. D., and Timmes, F. X. (2023). Modules for Experiments in Stellar Astrophysics (MESA): Time-dependent Convection, Energy Conservation, Automatic Differentiation, and Infrastructure. , 265(1):15.

Johnson, H. L. and Sandage, A. R. (1955). The galactic cluster M 67 and its significance for stellar evolution. , 121:616.

Kopal, Z. (1955). The classification of close binary systems. *Annales d'Astrophysique*, 18:379.

Kunimoto, M., Tey, E., Fong, W., Hesse, K., Shporer, A., Fausnaugh, M., Vanderspek, R., and Ricker, G. (2022). Quick-look Pipeline Light Curves for 5.7 Million Stars Observed Over the Second Year of TESS' First Extended Mission. *Research Notes of the American Astronomical Society*, 6(11):236.

Kwee, K. K. and van Woerden, H. (1956). A method for computing accurately the epoch of minimum of an eclipsing variable. , 12:327.

Landsman, W., Bohlin, R. C., Neff, S. G., O'Connell, R. W., Roberts, M. S., Smith, A. M., and Stecher, T. P. (1998). The Hot Stars of Old Open Clusters: M67, NGC 188, and NGC 6791. , 116(2):789–800.

Leigh, N. and Geller, A. M. (2012). Small-N collisional dynamics: pushing into the realm of not-so-small N. , 425(3):2369–2377.

Leigh, N. and Sills, A. (2011). An analytic technique for constraining the dynamical origins of multiple star systems containing merger products. , 410(4):2370–2384.

Leigh, N. W. C. and Geller, A. M. (2013). The dynamical significance of triple star systems in star clusters. , 432(3):2474–2479.

Leiner, E. M. and Geller, A. (2021). A Census of Blue Stragglers in Gaia DR2 Open Clusters as a Test of Population Synthesis and Mass Transfer Physics. , 908(2):229.

Leonard, P. J. T. (1989). Stellar Collisions in Globular Clusters and the Blue Straggler Problem. , 98:217.

Lightkurve Collaboration, Cardoso, J. V. d. M., Hedges, C., Gully-Santiago, M., Saunders, N., Cody, A. M., Barclay, T., Hall, O., Sagear, S., Turtelboom, E., Zhang, J., Tzanidakis, A., Mighell, K., Coughlin, J., Bell, K., Berta-Thompson, Z., Williams, P., Dotson, J., and Barentsen, G. (2018). Lightkurve: Kepler and TESS time series analysis in Python. Astrophysics Source Code Library, record ascl:1812.013.

Lu, P., Deng, L. C., and Zhang, X. B. (2010). Blue straggler formation via close binary mass transfer. , 409(3):1013–1021.

Mardling, R. A. and Aarseth, S. J. (2001). Tidal interactions in star cluster simulations. , 321(3):398–420.

Mathieu, R. D. and Latham, D. W. (1986). The spatial distribution of spectroscopic binaries and blue stragglers in the open cluster M67. , 92:1364–1371.

Mathieu, R. D. and Pols, O. R. (2025). Blue Stragglers and Friends: Initial Evolutionary Pathways in Close Low-Mass Binaries. , 63(1):467–512.

Mathys, G. (1991). The blue stragglers of M 67. , 245:467.

McCrea, W. H. (1964). Extended main-sequence of some stellar clusters. , 128:147.

Meibom, S. and Mathieu, R. D. (2005). A Robust Measure of Tidal Circularization in Coeval Binary Populations: The Solar-Type Spectroscopic Binary Population in the Open Cluster M35. , 620(2):970–983.

Morales, J. C., Gallardo, J., Ribas, I., Jordi, C., Baraffe, I., and Chabrier, G. (2010). The Effect of Magnetic Activity on Low-Mass Stars in Eclipsing Binaries. , 718(1):502–512.

Nelson, C. A. and Eggleton, P. P. (2001). A Complete Survey of Case A Binary Evolution with Comparison to Observed Algol-type Systems. , 552(2):664–678.

Paczyński, B. (1971). Evolutionary Processes in Close Binary Systems. , 9:183.

Paxton, B., Bildsten, L., Dotter, A., Herwig, F., Lesaffre, P., and Timmes, F. (2011). Modules for Experiments in Stellar Astrophysics (MESA). , 192:3.

Paxton, B., Cantiello, M., Arras, P., Bildsten, L., Brown, E. F., Dotter, A., Mankovich, C., Montgomery, M. H., Stello, D., Timmes, F. X., and Townsend, R. (2013). Modules for Experiments in Stellar Astrophysics (MESA): Planets, Oscillations, Rotation, and Massive Stars. , 208:4.

Paxton, B., Marchant, P., Schwab, J., Bauer, E. B., Bildsten, L., Cantiello, M., Dessart, L., Farmer, R., Hu, H., Langer, N., Townsend, R. H. D., Townsley, D. M., and Timmes, F. X. (2015). Modules for Experiments in Stellar Astrophysics (MESA): Binaries, Pulsations, and Explosions. , 220:15.

Paxton, B., Schwab, J., Bauer, E. B., Bildsten, L., Blinnikov, S., Duffell, P., Farmer, R., Goldberg, J. A., Marchant, P., Sorokina, E., Thoul, A., Townsend, R. H. D., and Timmes, F. X. (2018). Modules for Experiments in Stellar Astrophysics (MESA): Convective Boundaries, Element Diffusion, and Massive Star Explosions. , 234:34.

Paxton, B., Smolec, R., Schwab, J., Gautschy, A., Bildsten, L., Cantiello, M., Dotter, A., Farmer, R., Goldberg, J. A., Jermyn, A. S., Kanbur, S. M., Marchant, P., Thoul, A., Townsend, R. H. D., Wolf, W. M., Zhang, M., and Timmes, F. X. (2019). Modules for Experiments in Stellar Astrophysics (MESA): Pulsating Variable Stars, Rotation, Convective Boundaries, and Energy Conservation. , 243(1):10.

Perets, H. B. and Fabrycky, D. C. (2009). On the Triple Origin of Blue Stragglers. , 697(2):1048–1056.

Pols, O. R., Schröder, K.-P., Hurley, J. R., Tout, C. A., and Eggleton, P. P. (1998). Stellar evolution models for Z = 0.0001 to 0.03. , 298(2):525–536.

Portegies Zwart, S. F., McMillan, S. L. W., and Gieles, M. (2010). Young Massive Star Clusters. , 48:431–493.

Pribulla, T., Rucinski, S., Matthews, J. M., Kallinger, T., Kuschnig, R., Rowe, J. F., Guenther, D. B., Moffat, A. F. J., Sasselov, D., Walker, G. A. H., and Weiss, W. W. (2008). MOST satellite photometry of stars in the M67 field: eclipsing binaries, blue stragglers and δ Scuti variables. , 391(1):343–353.

Ricker, G. R., Winn, J. N., Vanderspek, R., Latham, D. W., Bakos, G. Á., Bean, J. L., Berta-Thompson, Z. K., Brown, T. M., Buchhave, L., Butler, N. R., Butler, R. P., Chaplin, W. J., Charbonneau, D., Christensen-Dalsgaard, J., Clampin, M., Deming, D., Doty, J., De Lee, N., Dressing, C., Dunham, E. W., Endl, M., Fressin, F., Ge, J., Henning, T., Holman, M. J., Howard, A. W., Ida, S., Jenkins, J. M., Jernigan, G., Johnson, J. A., Kaltenegger, L., Kawai, N., Kjeldsen, H., Laughlin, G., Levine, A. M., Lin, D., Lissauer, J. J., MacQueen, P., Marcy, G., McCullough, P. R., Morton, T. D., Narita, N., Paegert, M., Palle, E., Pepe, F., Pepper, J., Quirrenbach, A., Rinehart, S. A., Sasselov, D., Sato, B., Seager, S., Sozzetti, A., Stassun, K. G., Sullivan, P., Szentgyorgyi, A., Torres, G., Udry, S., and Villasenor, J. (2015). Transiting Exoplanet Survey Satellite (TESS). *Journal of Astronomical Telescopes, Instruments, and Systems*, 1:014003.

Sandage, A. R. (1953). The color-magnitude diagram for the globular cluster M 3. , 58:61–75.

Sanders, W. L. (1977). Membership of the open cluster M67. , 27:89–116.

Sandquist, E. L., Latham, D. W., Shetrone, M. D., and Milone, A. A. E. (2003). The Blue Straggler RS Canum Venaticorum Star S1082 in M67: A Detailed Light Curve and the Possibility of a Triple. , 125(2):810–824.

Sandquist, E. L. and Shetrone, M. D. (2003). Time Series Photometry of M67: W Ursae Majoris Systems, Blue Stragglers, and Related Systems. , 125(4):2173–2187.

Scott, N. J., Howell, S. B., Horch, E. P., and Everett, M. E. (2018). The NN-explore Exoplanet Stellar Speckle Imager: Instrument Description and Preliminary Results. , 130(987):054502.

Simoda, M. (1991). Detection of Variable Stars among Blue Stargglers in M67. *Information Bulletin on Variable Stars*, 3675:1.

Soberman, G. E., Phinney, E. S., and van den Heuvel, E. P. J. (1997). Stability criteria for mass transfer in binary stellar evolution. , 327:620–635.

Szentgyorgyi, A. H. and Furész, G. (2007). Precision Radial Velocities for the Kepler Era. In Kurtz, S., editor, *Revista Mexicana de Astronomia y Astrofisica Conference Series*, volume 28 of *Revista Mexicana de Astronomia y Astrofisica Conference Series*, pages 129–133.

Temmink, K. D., Pols, O. R., Justham, S., Istrate, A. G., and Toonen, S. (2023). Coping with loss. Stability of mass transfer from post-main-sequence donor stars. , 669:A45.

Tian, B., Deng, L., Han, Z., and Zhang, X. B. (2006). The blue stragglers formed via mass transfer in old open clusters. , 455(1):247–254.

Tran, K., Levine, A., Rappaport, S., Borkovits, T., Csizmadia, S., and Kalomeni, B. (2013). The Anticorrelated Nature of the Primary and Secondary Eclipse Timing Variations for the Kepler Contact Binaries. , 774(1):81.

van den Berg, M., Orosz, J., Verbunt, F., and Stassun, K. (2001). The blue straggler S 1082: A triple system in the old open cluster M 67. , 375:375–386.

van den Berg, M., Tagliaferri, G., Belloni, T., and Verbunt, F. (2004). A Chandra observation of the old open cluster M 67. , 418:509–523.

Vanderburg, A. and Johnson, J. A. (2014). A Technique for Extracting Highly Precise Photometry for the Two-Wheeled Kepler Mission. , 126(944):948.

Vanderburg, A., Latham, D. W., Buchhave, L. A., Bieryla, A., Berlind, P., Calkins, M. L., Esquerdo, G. A., Welsh, S., and Johnson, J. A. (2016). Planetary Candidates from the First Year of the K2 Mission. , 222(1):14.

Čokina, M., Fedurco, M., and Parimucha, Š. (2021). ELISa: A new tool for fast modelling of eclipsing binaries. , 652:A156.

Virtanen, P., Gommers, R., Oliphant, T. E., Haberland, M., Reddy, T., Cournapeau, D., Burovski, E., Peterson, P., Weckesser, W., Bright, J., van der Walt, S. J., Brett, M., Wilson, J., Millman, K. J., Mayorov, N., Nelson, A. R. J., Jones, E., Kern, R., Larson, E., Carey, C. J., Polat, İ., Feng, Y., Moore, E. W., VanderPlas, J., Laxalde, D., Perktold, J., Cimrman, R., Henriksen, I., Quintero, E. A., Harris, C. R., Archibald, A. M., Ribeiro, A. H., Pedregosa, F., van Mulbregt, P., and SciPy 1. 0 Contributors (2020). SciPy 1.0: fundamental algorithms for scientific computing in Python. *Nature Methods*, 17:261–272.

Virtanen, P., Gommers, R., Oliphant, T. E., Haberland, M., Reddy, T., Cournapeau, D., Burovski, E., Peterson, P., Weckesser, W., Bright, J., van der Walt, S. J., Brett, M., Wilson, J., Millman, K. J., Mayorov, N., Nelson, A. R. J., Jones, E., Kern, R., Larson, E., Carey, C. J., Polat, İ., Feng, Y., Moore, E. W., VanderPlas, J., Laxalde, D., Perktold, J., Cimrman, R., Henriksen, I., Quintero, E. A., Harris, C. R., Archibald, A. M., Ribeiro, A. H., Pedregosa, F., van Mulbregt, P., and SciPy 1.0 Contributors (2020). SciPy 1.0: Fundamental Algorithms for Scientific Computing in Python. *Nature Methods*, 17:261–272.

Völschow, M., Schleicher, D. R. G., Banerjee, R., and Schmitt, J. H. M. M. (2018). Physics of the Applegate mechanism: Eclipsing time variations from magnetic activity. , 620:A42.

Watson, C. A. and Dhillon, V. S. (2004). The effect of star-spots on eclipse timings of binary stars. , 351(1):110–116.

Zacharias, N., Finch, C. T., Girard, T. M., Henden, A., Bartlett, J. L., Monet, D. G., and Zacharias, M. I. (2013). The Fourth US Naval Observatory CCD Astrograph Catalog (UCAC4). , 145(2):44.

Zhao, J. L., Tian, K. P., Pan, R. S., He, Y. P., and Shi, H. M. (1993). Study of proper motions in the region of the open cluster M67 and membership of stars. , 100:243–261.